

Helical Fields and Filamentary Molecular Clouds

Jason D. Fiege and Ralph E. Pudritz

Dept. of Physics and Astronomy

McMaster University

1280 Main St. W., Hamilton, Ontario

L8S 4M1

email: fiege@physics.mcmaster.ca,

pudritz@physics.mcmaster.ca

15 August 2019

ABSTRACT

We study the equilibrium of pressure truncated, filamentary molecular clouds that are threaded by rather general helical magnetic fields. We first derive a new virial equation appropriate for magnetized filamentary clouds, which includes the effects of non-thermal motions and the turbulent pressure of the surrounding ISM. When compared with the data, we find that many filamentary clouds have a mass per unit length that is significantly reduced by the effects of external pressure, and that toroidal fields play a significant role in squeezing such clouds. We show that magnetized filaments that are initially in equilibrium are always stable in the sense of Bonnor (1956) and Ebert (1955). Radial collapse to a spindle-like configuration is possible only if the mass per unit length exceeds a critical value that depends on the magnetic field. The filamentary clouds in our sample appear to be well below this limit.

We also develop exact numerical MHD models of filamentary molecular clouds with more general helical field configurations than have previously been considered. We also examine the effects of the equation of state by comparing “isothermal” filaments, with constant *total* (thermal plus turbulent) velocity dispersion, with equilibria constructed using the pure logatropes of McLaughlin and Pudritz (1996).

Our theoretical models involve 3 parameters; two to describe the mass loading of the toroidal and poloidal fields, and a third that describes the radial concentration of the filament. We show that by using 3 observed quantities of filamentary clouds, namely, their observed line-widths, masses per unit length, and radii, our theoretical models can be strongly constrained. We perform a Monte Carlo exploration of our parameter space to determine which choices of parameters result in models that agree with the available observational constraints. We find that both equations of state result in equilibria that agree with the observational results. Moreover, we find that models with helical fields have more realistic density profiles than either unmagnetized models or those with purely poloidal fields; we find that most isothermal models have density distributions that fall off as $r^{-1.8}$ to r^{-2} , while logatropes have density profiles that range from r^{-1} to $r^{-1.8}$. This behaviour arises because of the dominance of the toroidal field in the outer parts of the clouds. We find that purely poloidal fields produce filaments with steep density gradients that not allowed by the observations.

Key words: ISM: magnetic fields – ISM: clouds – MHD

1 INTRODUCTION

Observations have revealed that most molecular clouds are filamentary structures that are supported by non-thermal, small-scale MHD motions of some kind, as well as large scale ordered magnetic fields (cf. Schleuning 1998). Never-

theless, virtually all theoretical models assume spheroidal geometry. While spheroidal models are a reasonable geometry for molecular cloud *cores*, these cannot adequately describe molecular clouds on larger scales. The goal of this paper is to fully develop a theory for filamentary molecular clouds including the effects of ordered magnetic fields. It is

our intent that this work should elevate filamentary clouds to the same level of understanding as that enjoyed by their spheroidal counterparts (cf. McKee et al. 1993). This is an important step in star formation theory because filamentary molecular clouds ultimately provide the initial conditions for star formation. A clear understanding of the initial conditions is necessary if we are to understand the processes by which clouds produce their star-forming cores.

Most theoretical models for self-gravitating filaments have featured magnetic fields that are aligned with the major axis of the filaments (cf. Nagasawa 1987; Gehman, Adams, & Watkins. 1996). However, observations suggest that some molecular clouds may be wrapped by helical fields (Bally 1987; Heiles 1987). There is also some observational evidence for helical fields in HI filaments towards the Galactic high latitude clouds (Gomez de Castro, Pudritz, & Bastien 1997). In fact, helical fields represent the most general magnetic field configuration allowed if cylindrical symmetry is assumed. A few authors have previously modeled filamentary clouds with helical fields, but they concentrate only on “special” helical field solutions that can be solved analytically (cf. Nakamura, Hanawa, & Nakano 1993; Hanawa et al., 1993). These models are isothermal with the field components finely tuned so that the density distribution is a simple rescaling of the Ostriker (1964) solution for unmagnetized isothermal filaments. They are also unconstrained by observational data. Our models of filamentary molecular clouds with helical magnetic fields are more general because we do not restrict ourselves to an isothermal equation of state (EOS), and we employ field configurations that have a non-trivial effect on the density distribution. Moreover, our models are well understood from the perspective of a new virial equation appropriate for filamentary equilibria.

The role of the external pressure on filaments has been almost completely ignored by previous models of filamentary clouds. As we discuss in Section 2.3, real molecular clouds are always truncated at some finite radius by the pressure of the external medium; by ignoring the role of the external pressure, most previous models have no hope of adequately describing real filamentary clouds. The lack of pressure truncation allows the models of Nakamura et al. (1993) and Gehman et al. (1996) to extend to infinite radius. Particularly problematic are Gehman’s et al. logatropic models which possess infinite mass per unit length as a result. We have included the effects of external pressure in our models and have made at least a first attempt to constrain our models using observational results gathered from the literature. We are, in fact, only aware of two models that have previously included external pressure. Viala (1974) constructed models of polytropic filaments and other equilibria. He considered the effects of pressure truncation but did not include magnetic fields. Chandrasekhar and Fermi (1953) analysed the stability of incompressible filaments with longitudinal magnetic fields. Their equilibria are both magnetized and truncated, but their assumption of incompressibility is unrealistic. By including a very general helical magnetic field and external pressure, both of which we constrain observationally, we have constructed much more complete models of filamentary molecular clouds.

Why should filamentary molecular clouds containing helical magnetic fields be considered? Large scale maps of the HI gas in the Milky Way reveal a highly filamentary

and shell-dominated structure that is probably produced by coherent supernova explosions and subsequent super-shell formation in the interstellar medium (Heiles 1997). It is possible that many filamentary molecular clouds condense out of dense HI filaments that form as the swept-up gas in the walls of these large, shocked and strongly magnetized shells, cools. Even if molecular filaments form with an initially axial magnetic field, a helical field is plausibly generated by any kind of shear motion (such as subsequent oblique shocks, torsional Alfvén waves, etc.) that twists the field lines at any point along such shell walls.

It is not the purpose of this paper to examine how helical fields could be generated. The main point of this work is that, having recognized that most molecular clouds are undoubtedly filamentary, magnetized, and truncated by an external pressure, it is of considerable importance to investigate equilibrium models of molecular clouds that contain general helical fields and pressure truncation. We employ two main approaches in our theoretical analysis. Firstly, we derive a general virial equation appropriate for pressure-truncated filamentary molecular clouds, which we use to understand the roles of gravity, pressure, and the magnetic field in the overall quasi-equilibrium of filamentary clouds. Secondly, we develop numerical MHD equilibrium models that can be compared with the internal structure of real clouds.

Our virial analysis demonstrates that poloidal fields always help to support the gas against self-gravity, while toroidal fields squeeze the gas by the “hoop stress” of their curved field lines. Helical fields may either support or help to confine the gas, depending on whether the poloidal or toroidal field component is dominant. We have established strong constraints on our models using the available observational data. By comparing with data gathered from the literature, our virial analysis demonstrates that many filamentary clouds have internal velocity dispersions that are too high for clouds to be bound by self-gravity and external pressure alone; thus, we find evidence that toroidally dominated helical fields may wrap many filamentary clouds. We show, in fact, that it is very difficult to understand observed clouds without the notion of helical fields and the confining hoop stresses that they exert upon their molecular gas. Our arguments for the existence of helical fields are somewhat indirect in that they rely entirely on global virial properties of filamentary clouds, namely mass per unit length, average velocity dispersion, and radius. Our virial analysis is necessary because the data that is necessary to compare with our numerical models is presently quite scarce.

Having found evidence for helical fields from our virial analysis, we construct numerical MHD models of filamentary clouds in order to investigate the internal structure of models that are allowed by the data. Ostriker (1964) investigated the equilibrium of unmagnetized isothermal filaments; he found that the density varies as $\sim r^{-4}$ in the outer regions. However, this solution is much too steep to account for the observed density profiles in molecular clouds. For example, Alves et al. (1998, hereafter A98) and Lada, Alves, and Lada (1998, hereafter LAL98) use extinction measurements of background starlight in the near infra-red to find r^{-2} density profiles for the filamentary clouds L977 and IC 5146. *It is noteworthy that our isothermal models with helical magnetic fields always produce density profiles that fall off as $r^{-1.8}$ to r^{-2} , in excellent agreement with the data.* We show

that the *toroidal* field component is responsible for the more realistic behaviour, and that purely poloidal fields result in density profiles that fall even more rapidly than r^{-4} . We also consider the pure logatropes of McLaughlin and Pudritz (1996, hereafter MP96) as a possible effective EOS for the gas, and find that unmagnetized logatropic filaments have a very shallow $\sim r^{-1}$ density profile. With the addition of a helical magnetic field, the density falls off as r^{-1} to $r^{-1.8}$; thus, logatropic filaments typically have more shallow density profiles, but they cannot be ruled out altogether by the existing data.

A summary of our paper is as follows. We first present the results of virial analysis of self-gravitating, pressure truncated, filamentary clouds containing both poloidal and toroidal field (Section 2). In Section 3, we follow this up with a detailed analysis of the equations of magnetohydrostatic equilibrium describing self-gravitating filaments and discuss important analytic solutions to these. A full numerical treatment of the equations is given in Section 4 where we also constrain our 3-parameter models with a wide variety of filamentary cloud data. We discuss these results in Section 5 and summarize in Section 6.

2 VIRIAL ANALYSIS FOR FILAMENTARY MOLECULAR CLOUDS

The tensor virial theorem is written in its most general form as

$$\begin{aligned} \frac{1}{2} \frac{d^2 I_{ik}}{dt^2} &= 2T_{ik} + \delta_{ik} \left[\int_V PdV + M_V \right] + W_{ik} - 2M_{ik} \\ &+ \int_S x_k \left(\frac{B_i B_j}{4\pi} dS_j - \frac{B^2}{8\pi} dS_i \right) - \int_s P x_k dS_i, \end{aligned} \quad (1)$$

(Chandrasekhar 1961) where we work in Cartesian coordinates x_i , and the integration is over the volume V of the cloud bounded by surface S . Here, P is the *total* pressure (with both thermal and non-thermal contributions) and I_{ik} , T_{ik} , W_{ik} , and M_{ik} are respectively the Cartesian tensors for moment of inertia, kinetic energy, gravitational potential, and magnetic energy. The pressure and magnetic field both contribute bulk terms that support the cloud and surface terms that confine the gas. The magnetic term M_V is just the bulk component of the magnetic energy:

$$M_V = \frac{1}{8\pi} \int B^2 dV \quad (2)$$

where B is the magnitude of the magnetic field. The tensor components are given by

$$\begin{aligned} I_{ik} &= \int dV \rho x_i x_k \\ T_{ik} &= \frac{1}{2} \int dV \rho v_i v_k \\ W_{ik} &= - \int dV \rho x_k \frac{\partial \Phi}{\partial x_i} \\ M_{ik} &= \frac{1}{8\pi} \int dV B_i B_k, \end{aligned} \quad (3)$$

where ρ is density, P is pressure, v_i and B_i are components of velocity and magnetic field, and Φ is the gravitational potential.

The virial theorem is most often stated in its *scalar* form, which is obtained by taking the trace of equation 1. However, we are concerned with applying the virial theorem to a filamentary cloud idealized as an infinite cylinder whose axis we assume to be aligned with the z (x_3) direction. We replace the usual trace with just the sum of the x and y (11 and 22) components because we are only concerned with the equilibrium in the radial direction. The full derivation of our virial equation appears in Appendix A; after carrying out the manipulations therein, we obtain

$$0 = 2 \int PdV - 2P_S \mathcal{V} + \mathcal{W} + \mathcal{M}, \quad (4)$$

where the gravitational energy per unit length is given by

$$\mathcal{W} = - \int \rho r \frac{\partial \Phi}{\partial r} dV. \quad (5)$$

and \mathcal{M} is the sum of all magnetic terms (including surface terms):

$$\mathcal{M} = \frac{1}{4\pi} \int B_z^2 dV - \left(\frac{B_{zS}^2 + B_{\phi S}^2}{4\pi} \right) \mathcal{V}. \quad (6)$$

As we discuss in Appendix A, this equation is appropriate for a non-rotating, self-gravitating, filamentary molecular cloud whose length greatly exceeds its radius. *For the remainder of this paper, all quantities written with a subscript S are to be evaluated at the surface of the filament*; thus we write that our filament is truncated by an external pressure P_S at radius R_S . We further reserve *calligraphic symbols* for quantities evaluated per unit length; \mathcal{W} is the gravitational energy per unit length since there are no external gravitational fields and \mathcal{V} is actually the volume per unit length, or cross-sectional area πR_S^2 , of the filament. As we shall now show, \mathcal{W} can be evaluated *exactly* for a filament of *arbitrary* internal structure and equation of state. The mass per unit length m of the filament is obtained by simply integrating the density over the cross-sectional area:

$$m = 2\pi \int r \rho(r) dr. \quad (7)$$

Poisson's equation in cylindrical coordinates takes the form

$$\frac{1}{r} \frac{d}{dr} \left(r \frac{d\Phi}{dr} \right) = 4\pi G \rho. \quad (8)$$

By integrating, we find that the mass per unit length interior to radius r can be written as

$$m(r) = \frac{1}{2G} r \left. \frac{d\Phi}{dr} \right|_r. \quad (9)$$

Using this result in equation 5, the gravitational energy per unit length can be transformed into an integral over the mass per unit length:

$$\mathcal{W} = -2G \int_0^m m' dm' = -m^2 G. \quad (10)$$

It is remarkable that the gravitational energy per unit length takes on the same value *regardless of the equation of state, magnetic field, or internal structure of the cloud*. The only requirements are those of virial equilibrium and cylindrical geometry. McCrea (1957) gave an approximate formula for the gravitational energy per unit length as $\mathcal{W} = -am^2 G$ (where a is a constant of order unity) based on dimensional

considerations; thus, our exact result gives $a = 1$ for all cylindrical mass distributions.

By considering a long filament of finite mass M and length L , we find that the gravitational energy scales quite differently for filaments and spheroids:

$$\begin{aligned} W_{cyl} &= -\frac{GM^2}{L} \\ W_{sphere} &= -\frac{3}{5}a\frac{GM^2}{R}, \end{aligned} \quad (11)$$

where a depends on the detailed shape and internal structure for spheroids. It is of fundamental importance that the gravitational energy scales with radius for spheroids, but not for filaments. McCrea (1957) used this point to argue that filaments possess stability properties quite contrary to those of spheroidal equilibria. For spheroids, which best describe molecular cloud cores, the gravitational energy scales as $\sim R^{-1}$. As long as the core is magnetically subcritical, there always exists a critical external pressure beyond which the gravitational energy must dominate over the pressure support. The equilibrium is unstable to gravitational collapse past this critical external pressure. On the other hand, the gravitational energy of a filament is unaffected by a change in radius. Thus, the gravitational energy remains constant during any radial contraction caused by increased external pressure. If the filament is initially in equilibrium, gravity can never be made to dominate by squeezing the filament; all hydrodynamic filaments *initially in equilibrium* are stable in the sense of Bonnor (1956) and Ebert (1955). In Section 2.5 we show that the toroidal component of the magnetic field behaves much like an effective gravity for magnetized filaments. We address the Bonnor-Ebert stability properties of uniform magnetized filaments in Section 2.6 and general magnetized filaments in Section 3.3.

The virial theorem for filaments (equation 4) is best used to study the global properties of filamentary molecular clouds. It is useful to define the average density, pressure, and magnetic pressure within the cloud as

$$\begin{aligned} \langle \rho \rangle &= \frac{m}{V} \\ \langle P \rangle &= \frac{\int_V P dV}{V} \\ \langle P_{mag} \rangle &= \frac{1}{8\pi V} \int_V B_z^2 dV. \end{aligned} \quad (12)$$

Quite generally, we may write the effective pressure inside a molecular cloud as $P = \sigma^2 \rho$, where σ is the total velocity dispersion. *We emphasize that all of our models regard σ as representing the total velocity dispersion, including both thermal and non-thermal components. It is particularly important to note that when we describe an equation of state as “isothermal”, we really mean that the total velocity dispersion is constant.* The average squared velocity dispersion is defined simply as

$$\langle \sigma^2 \rangle = \frac{\langle P \rangle}{\langle \rho \rangle} = \frac{\int_V \sigma^2 \rho dV}{\int_V \rho dV}, \quad (13)$$

where the average has been weighted by the mass as in MP96.

With the above definitions, we easily derive a useful form of our virial equation (equation 4):

$$\frac{P_S}{\langle P \rangle} = 1 - \frac{m}{m_{vir}} \left(1 - \frac{\mathcal{M}}{|\mathcal{W}|} \right), \quad (14)$$

where \mathcal{M} and \mathcal{W} are the total magnetic and kinetic energies per unit length defined in equations 5 and 6, and m_{vir} is the virial mass per unit length defined by

$$m_{vir} = \frac{2\langle \sigma^2 \rangle}{G}. \quad (15)$$

We note that m_{vir} is analogous to the the virial mass

$$M_{vir} = \frac{5R\langle \sigma^2 \rangle}{G} \quad (16)$$

normally defined for spheroidal equilibria. Using the definition of the average magnetic pressure given in equation 12, we may write the total magnetic energy as

$$\mathcal{M} = 2(\langle P_{mag} \rangle - P_{mag,S})V. \quad (17)$$

Using this result, along with the expression for the gravitational energy per unit length (equation 10) in equation 14, we obtain another useful for our virial equation after some algebraic manipulations:

$$\frac{P_S}{\langle P \rangle} = 1 - \frac{m}{m_{vir}} + \left(\frac{\langle P_{mag} \rangle - P_{mag,S}}{\langle P \rangle} \right), \quad (18)$$

where $P_{mag,S}$ is the total magnetic pressure evaluated at the surface of the cloud:

$$P_{mag,S} = \frac{B_{zS}^2 + B_{\phi S}^2}{8\pi}. \quad (19)$$

Referring to our virial equation 18, we note that only the poloidal component of the magnetic field contributes to the magnetic pressure support of the cloud through $\langle P_{mag} \rangle$. It is also clear that the toroidal field enters into equation 18 only as a surface term, through $P_{mag,S}$, which helps to confine the cloud by the “pinch effect” well known in plasma physics. The magnetic force per unit volume due to the toroidal field is

$$\mathcal{F}_{mag} = -\frac{d}{dr} \left(\frac{B_{\phi}^2}{8\pi} \right) - \frac{B_{\phi}^2}{4\pi r}. \quad (20)$$

This equation represents a competition between the usual expansive magnetic pressure term and confinement of the plasma by the “hoop stress” of the curved toroidal flux tubes. It is easily seen that any field that falls off less steeply than r^{-1} has a net confining effect. Fields that fall off more steeply than r^{-1} cannot be produced by any reasonable distribution of poloidal current without a current reversal.

All magnetic fields, whether poloidal, toroidal, or of a more complex geometry, are associated with currents that flow within molecular clouds and the surrounding ISM. For a filamentary cloud wrapped by a helical field, the toroidal field component implies the existence of a poloidal current that flows along the filament. A toroidal field, along with its associated current, arises naturally if one end of a filamentary cloud threaded by a poloidal field is twisted relative to the other end. A natural question is whether a return current outside of the filamentary cloud completes the “circuit”, or whether the poloidal current connects to larger scale structures in the ISM. The answer to this question will likely depend on the mechanisms by which filaments form, which might be addressed by future analysis. If the current returns

as a thin current sheet flowing along the surface of the filament, the toroidal field at the surface would be nullified, and so would its confining effects. As we show in Section 2, this would make the available data very difficult to understand, indeed. However, if the return current is diffuse and extended throughout the surrounding gas, as in the case of protostellar jets (Ouyed & Pudritz 1997), there would be a net magnetic confinement of the filament, which is consistent with the observations.

2.1 Unmagnetized Filaments

From equation 14, we see that unmagnetized clouds obey the following linear relation:

$$\frac{P_S}{\langle P \rangle} = 1 - \frac{m}{m_{vir}}. \quad (21)$$

This equation is exact for any unmagnetized filamentary cloud in virial equilibrium regardless of the underlying equation of state or details of the internal structure. Since equation 21 contains only quantities that are observable, we have derived an important diagnostic tool for determining whether or not filamentary clouds contain dynamically important ordered magnetic fields. We will make extensive use of this fact in Section 2.7 where we directly compare our models with existing data.

We can use equation 21 to obtain the critical mass per unit length m_h for self-gravitating hydrostatic filaments. *The critical mass per unit length is the maximum mass per unit length for which radial equilibrium can be obtained.* Since $P_S/\langle P \rangle \geq 0$, the critical mass per unit length is given by

$$m_h = \lim_{P_S \rightarrow 0} m_{vir} = \lim_{P_S \rightarrow 0} \frac{2\langle \sigma^2 \rangle}{G} \quad (22)$$

regardless of the EOS or internal density structure of the filament. An approximate formula for m_h was first given by McCrea (1957) for the case of isothermal filaments. From equation 22, we note that the virial mass per unit length m_{vir} plays the role of the critical mass per unit length for unmagnetized filaments; we shall find in Section 2.2 that this is not generally the case for magnetized filamentary clouds. (We note that $\langle \sigma^2 \rangle$ is implicitly a function of P_S since $\langle \sigma^2 \rangle \propto \int_V \sigma^2 \rho dV$; the surface pressure P_S controls the truncation radius, and hence the cross-sectional area V .) When the mass per unit length exceeds m_h , no equilibrium is possible and radial collapse must result. It is important to realize that m_{vir} is an *observable* quantity for a pressure truncated filamentary molecular cloud. On the other hand, m_h *cannot* be directly obtained since it is proportional to the velocity dispersion averaged (see equation 13) out to the radius of vanishing external pressure. In general, this extrapolation can only be accomplished by modeling, which in turn requires *a priori* knowledge of the EOS of the gas. Nevertheless, $m_h \approx m_{vir}$ for clouds that are governed by an approximately “isothermal” EOS, with constant *total* velocity dispersion.

2.2 Magnetized Filaments

When there is a magnetic field present in a filamentary molecular cloud, the critical mass per unit length is signif-

icantly modified from the result obtained for unmagnetized clouds in the previous Section. Considering the maximum possible mass per unit length allowed by equation 14, we find that the critical mass per unit length for magnetized filamentary clouds is given by

$$m_{mag} = \lim_{P_S \rightarrow 0} \frac{m_{vir}}{1 - \mathcal{M}/\mathcal{W}} = \frac{m_h}{1 - \mathcal{M}/\mathcal{W}}, \quad (23)$$

where \mathcal{M} and \mathcal{W} are the total magnetic and gravitational energies per unit length given by equations 17 and 10. We recall that \mathcal{M} may be either positive or negative, depending on whether the poloidal or the toroidal field dominates the overall magnetic energy. *In general, we find that poloidal fields increase the critical mass per unit length beyond m_h for hydrostatic filaments, while toroidal fields reduce the critical mass per unit length below m_h .* Physically, the reason for this behaviour is that the poloidal field helps to support the cloud radially against self-gravity, thus allowing greater masses per unit length to be supported. The opposite is true for the toroidal field component, which works with gravity in squeezing the cloud radially. Regardless of which field component is dominant, we may combine equation 23 with our virial equation 14 to obtain

$$\frac{m}{m_{mag}} = 1 - \frac{P_S}{\langle P \rangle}. \quad (24)$$

Therefore, it is the ratio of the external pressure to the mean internal pressure that controls how far a magnetized filamentary cloud is from its critical configuration.

We may constrain the critical mass per unit length for a filamentary cloud if we have additional information regarding the strengths of the poloidal and toroidal field components. Writing equation 18 in the limit of vanishing external pressure, the *magnetic* critical mass per unit length is given by

$$m_{mag} = m_h \left\{ 1 + \left[\frac{\langle P_{mag} \rangle - P_{mag,S}}{\langle P \rangle} \right] \right\}. \quad (25)$$

Since molecular clouds are in approximate equipartition between their magnetic and kinetic energies (Myers and Goodman 1988a,b, Bertoldi and McKee 1992), $\langle P_{mag} \rangle$ is not likely to greatly exceed $\langle P \rangle$. Therefore, it is unlikely that the magnetic critical mass per unit length m_{mag} would exceed the hydrostatic critical mass per unit length m_h by more than a factor of order unity.

It is interesting to note that the toroidal field has no effect on the critical mass per unit length m_{mag} if B_ϕ vanishes at the surface of the filament in the limit of zero external pressure. While this is generally true for untruncated isothermal filaments, which are of infinite radial extent, it is generally not true for logatropic filaments. Logatropic filaments are “self-truncating” in the sense that they cannot extend past the radius defined by $P_S = 0$ and $\rho_S = \rho_c \exp(-1/A)$. Thus, the critical mass per unit length is *decreased* by the addition of a toroidal field for logatropic filaments, but *unaffected* for isothermal filaments.

2.3 Surface Pressures on Molecular Filaments

Molecular clouds are surrounded by the atomic gas of the interstellar medium (ISM). Like the molecular gas itself, the total pressure of the ISM is dominated by its non-thermal

component, which is due to turbulent motions in the gas. The external pressure is extremely important to our analysis since it both truncates molecular clouds at finite radius and helps to confine the clouds against their own internal pressures (see equation 14). Boulares and Cox (1990) have estimated the *total* pressure (with thermal plus turbulent contributions) of the interstellar medium to be on the order of 10^4 K cm^{-3} . However, some molecular clouds are associated with HI complexes, whose pressures are typically an order of magnitude higher than the general ISM (Chromey, Elmegreen, & Elmegreen 1989). Intermediate cases probably exist, in which molecular clouds are surrounded by a relatively thin envelope of atomic gas (Elmegreen 1993). In this case, the pressure at the surface of the molecular cloud is substantially increased by the weight of the atomic gas on top; Elmegreen (1993) has estimated this pressure to be a few times 10^4 K cm^{-3} . Therefore, we will be absolutely conservative by assuming that the external pressure on molecular clouds is in the range of $10^{4-5} \text{ K cm}^{-3}$. This assumption almost certainly brackets the real pressure exerted on molecular clouds by imposing the total (*thermal plus turbulent*) pressure of the ISM as a lower bound, and the pressure of large HI complexes as the upper bound.

While the above pressure estimate is appropriate for most filamentary clouds, which are truncated directly by the pressure of the surrounding atomic gas, we must note that a second type of filament exists, in which a dense molecular filament is deeply embedded in a molecular cloud of irregular or spheroidal geometry. The best example of this type of filament is the \mathcal{J} -shaped filament in the Orion A cloud, which has been mapped in ^{12}CO , ^{13}CO , and $C^{18}\text{O}$ by Castets et al. (1990) and Dutrey et al. (1991, 1993). The filament has a mass of $\sim 7500 M_\odot$ and is surrounded by an envelope containing $\sim 3500 M_\odot$ of molecular gas within their ^{12}CO map. The molecular envelope blends with the Orion A cloud, which has a total mass of $\sim 10^5 M_\odot$ (Maddalena 1986) and does not share the filament's cylindrical geometry. Therefore, we consider the gas traced by ^{12}CO as the source of external pressure that truncates the filament. The surface pressure on the filament can be obtained from estimates of the envelope's density and velocity dispersion; from the results given by Maddalena, we obtain $P_S = 1.3 \times 10^5 \text{ K cm}^{-3}$

2.4 Virial Relations for Filaments

In this section we derive the virial relations for filamentary molecular clouds analogous to the well known relations for spheroidal clouds (Chièze 1987; Elmegreen 1989; MP96). Using equation 10 in our virial equation for filamentary clouds (equation 4), we write

$$0 = 2m\langle\sigma^2\rangle - 2P_S V - am^2 G + \mathcal{M} \quad (26)$$

We have shown in Section 2 that the constant a is exactly unity for any filament but we retain the constant in order to more directly compare with the corresponding expressions for spheroidal clouds. Equation 26 can be rewritten as

$$\alpha_{mag} = a \frac{1 - \mathcal{M}/|\mathcal{W}|}{1 - P_S/\langle P \rangle} \equiv \frac{m_{vir}}{m} \quad (27)$$

where we have introduced the *observable* virial parameter α_{mag} for filamentary clouds analogous to that of Bertoldi and McKee (1992, hereafter BM92). We may also write

	C_m	C_R	C_ρ	C_Σ
filament	2	$\sqrt{\frac{2}{\pi}}$	1	$\sqrt{\frac{\pi}{2}} \sec i$
spheroid	$\frac{5}{2}$	$5\sqrt{\frac{3}{20\pi}}$	1	$\sqrt{\frac{20}{3\pi}}$

Table 1. The coefficients of the virial relations given in equations 30. We have included a correction $\sec i$ for the projected surface density of filamentary equilibria and defined the effective mass per unit length for a sphere as $m_{sphere} = M/(2R)$.

$$\alpha_{mag} = \alpha_{non} \left(1 - \frac{\mathcal{M}}{|\mathcal{W}|} \right), \quad (28)$$

where α_{non} is just α_{mag} evaluated in the unmagnetized limit:

$$\alpha_{non} = \frac{a}{1 - P_S/\langle P \rangle}. \quad (29)$$

Equations 27 and 29 are easily solved for the mass per unit length m , radius R_S , average density $\langle\rho\rangle$, and surface density Σ . In order to compare with the corresponding results for spheroidal magnetized equilibria (See MP96), we present the results as general expressions with the coefficients written in table 1:

$$\begin{aligned} m &= C_m \frac{\langle\sigma^2\rangle}{\alpha_{mag} G} \\ R &= C_R \left(\frac{\alpha_{non} - a}{\alpha_{non}} \right)^{1/2} \frac{1}{\alpha_{mag}^{1/2}} \frac{\langle\sigma^2\rangle}{(GP_S)^{1/2}} \\ \langle\rho\rangle &= C_\rho \left(\frac{\alpha_{non}}{\alpha_{non} - a} \right) \frac{P_S}{\langle\sigma^2\rangle} \\ \Sigma &= C_\Sigma \frac{1}{\alpha_{mag}^{1/2}} \left(\frac{\alpha_{non}}{\alpha_{non} - a} \right)^{1/2} \left(\frac{P_S}{G} \right)^{1/2}. \end{aligned} \quad (30)$$

We have included a correction for the inclination i of the filament the the plane of the sky; this only affects the expression for the surface density. These expressions are remarkably similar to those for spheroidal clouds, retaining identical functional forms and differing only by coefficients of order unity. Of course, the mass per unit length of a filament cannot be compared directly to the mass of a spheroid. However, if we define an effective mass per unit length by taking $m_{sphere} = M/(2R)$, the resulting expression again differs from ours by only a numerical factor of order unity. Our result is an indication of the robustness of the virial theorem in dealing with different geometries. It is very reassuring that the corrections are not severe, since the virial theorem appropriate for spheroids has often been applied by observers to clouds that are intrinsically filamentary.

2.5 An Idealized Model: Uniform Magnetized Filaments

It is illustrative to consider the following idealized model for a filamentary molecular cloud with a helical magnetic field. We consider a cloud of uniform density threaded by a constant poloidal magnetic field that drops to zero at the cloud boundary. The simplest toroidal field geometry is that associated with a constant poloidal current density within the filament. This corresponds to a toroidal field B_ϕ that increases as $\sim r$ within the filament and falls off as $\sim r^{-1}$ in the external medium.

Our choice of magnetic field structure actually corresponds to that of constant poloidal and toroidal flux to mass ratios Γ_z and Γ_ϕ . The meanings of the flux to mass ratios are illustrated in Figure 1, and are defined in the following way. It is customary, for the poloidal field, to specify the *flux to mass ratio* throughout the cloud, which can in principle vary throughout the cloud. However, it is more appropriate to specify the ratio of poloidal flux to the mass per unit length for an infinite filament. Consider a bundle of poloidal field lines passing through a small cross-sectional area of the filament $\delta\mathcal{V}$. The magnetic flux passing through the surface is $B_z\delta\mathcal{V}$, while the mass per unit length is $\rho\mathcal{V}$. Thus, the poloidal flux to mass ratio is

$$\Gamma_z = \frac{B_z}{\rho}. \quad (31)$$

Is there an analogous quantity for the toroidal component of the field? In fact the *toroidal* flux has been defined and is commonly used in plasma physics (Bateman 1978). Here, we consider a bundle of toroidal flux lines with cross-sectional area δA that form a closed ring of radius r centred on the axis of the filament. The mass enclosed by the ring is $2\pi r\delta A$. Thus, we may define the toroidal flux to mass ratio (per radian) as

$$\Gamma_\phi = \frac{B_\phi}{r\rho}. \quad (32)$$

The simplest field configuration is that of constant Γ_z and Γ_ϕ . We note that constant Γ_ϕ results naturally if a filament of constant Γ_z and length L is twisted uniformly through an angle ϕ . Then

$$\frac{B_\phi}{B_z} = \frac{r\phi}{L}, \quad (33)$$

which leads to the result

$$\Gamma_\phi = \left(\frac{\phi}{L}\right) \Gamma_z. \quad (34)$$

We shall always assume constant Γ_z and Γ_ϕ for the remainder of this paper.

With the assumption of constant density and the above definitions of Γ_z and Γ_ϕ , equation 18 can be expanded to give

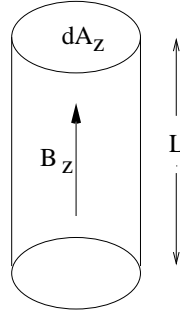
$$0 = \left(\sigma^2 - \frac{P_S}{\rho} + \frac{\Gamma_z^2 \rho}{8\pi}\right) - m \left(\frac{G}{2} + \frac{\Gamma_\phi^2}{8\pi^2}\right). \quad (35)$$

The critical mass per unit length is obtained by setting $P_S = 0$:

$$m_{mag} = \frac{2\sigma^2 + \Gamma_z^2 \rho / 4\pi}{G + \Gamma_\phi^2 / 4\pi^2}. \quad (36)$$

The effects of external pressure and the magnetic field are transparent in this simple model. Pressure and the poloidal field cooperate in supporting the cloud. On the other hand, the toroidal field enters into equation 35 in concert with gravity. A filamentary cloud with a helical field would be confined jointly by gravity, external pressure, and the pinch of the toroidal field. Without prior knowledge of the field strength and direction (by molecular Zeeman and polarization observations), the cloud may *appear* to be unbound by gravity alone. Other authors have previously reached similar conclusions for the clouds of Rho Ophiuchus (Loren 1989b) and clumps in various molecular clouds (BM92).

Poloidal flux/mass ratio
(per unit length)

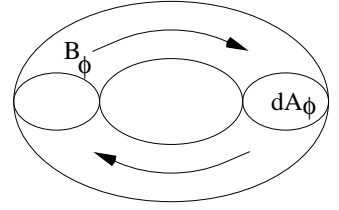


mass: $dM = \rho L dA$

flux: $d\Phi_z = B_z dA_z$

$$\Gamma_z = \frac{B_z}{\rho}$$

Toroidal flux/mass ratio
(per radian)



mass: $dM = 2\pi r \rho dA$

flux: $d\Phi_\phi = B_\phi dA$

$$\Gamma_\phi = \frac{B_\phi}{r \rho}$$

Figure 1. A schematic illustration of the poloidal and toroidal flux to mass ratios introduced in equations 31 and 32.

2.6 Bonnor-Ebert Stability of Uniform Magnetized Filaments

We have shown, in Section 2, that all hydrodynamic filaments, which are initially in equilibrium, are stable in the sense of Bonnor (1956) and Ebert (1955). In this section, we examine the Bonnor-Ebert stability of uniform *magnetized* filaments. We begin by considering a radial perturbation of a uniform filament in which the mass per unit length and the velocity dispersion are conserved. Solving equation 35 for the external pressure, we easily obtain

$$P_S = \frac{c_\phi}{\mathcal{V}} + \frac{c_z}{\mathcal{V}^2}, \quad (37)$$

where

$$\begin{aligned} c_\phi &= m\sigma^2 - m^2 \left(\frac{G}{2} + \frac{\Gamma_\phi^2}{8\pi} \right) \\ c_z &= \frac{m^2 \Gamma_z^2}{8\pi}. \end{aligned} \quad (38)$$

The equilibrium is unstable in the sense of Bonnor and Ebert for any P_S and \mathcal{V} for which

$$\frac{dP_S}{d\mathcal{V}} > 0. \quad (39)$$

Taking this derivative and simplifying using equations 37, 38, 31, and 12, we obtain

$$\frac{dP_S}{d\mathcal{V}} = -\frac{1}{\mathcal{V}} (P_S + P_{mag}) < 0. \quad (40)$$

Thus, equation 39 is *never* satisfied for any choice of \mathcal{V} and P_S . Unlike spheroidal clouds, *all uniform filaments in equilibrium (having $m \leq m_{mag}$) are stable in the sense of Bonnor and Ebert.* We extend this proof to the more general case of non-uniform magnetized filaments of arbitrary EOS in Section 3.3.

2.7 Comparison With Observations

The effect of an arbitrary helical magnetic field on the *global* properties of the cloud is entirely determined by equation 14. Thus, the magnetic field affects the global properties of filaments only through the dimensionless virial parameter $\mathcal{M}/|\mathcal{W}|$. We note that this equation holds true for a filamentary cloud of arbitrary EOS and helical field configuration since it is based on our virial results. The virial quantity $\mathcal{M}/|\mathcal{W}|$ provides a very convenient index of whether a cloud is poloidally or toroidally dominated and to what degree. For clouds with positive $\mathcal{M}/|\mathcal{W}|$, the net effect of the magnetic field is to provide support and the field is *poloidally dominated*. When $\mathcal{M}/|\mathcal{W}|$ is negative, the net effect of the field is confinement by the pinch of the toroidal field, and the field is *toroidally dominated*. Since \mathcal{M} is directly compared to the gravitational energy $|\mathcal{W}|$, the magnitude of our virial parameter provides an immediate indication of the importance of the ordered field to the dynamics of the cloud. In Figure 2, we have used equation 14 to draw contours of constant $\mathcal{M}/|\mathcal{W}|$ as a function of m/m_{vir} and $P_S/\langle P \rangle$. The $\mathcal{M}/|\mathcal{W}| = 0$ (dotted) line represents all helical field configurations, including the unmagnetized special case, which have a neutral effect on the global structure of the cloud. Thus, we see that the diagram is divided into poloidally dominated (dashed lines) and toroidally dominated (solid lines) regions.

Since both m/m_{vir} and $P_S/\langle P \rangle$ are *observable* quantities, we can constrain our models by locating individual filamentary clouds on this diagram. However, we must first compute m/m_{vir} and $P_S/\langle P \rangle$ for each cloud by the following steps. For each filament, we have found values for the mass, length, radius, and average linewidth from molecular line observations in the literature (see table 2 for references). The mass per unit length m is obtained by dividing the mass of the filament by its length allowing for inclination effects by conservatively assuming all filaments to be oriented within 45° of the plane of the sky. Since the emitting molecule (usually ^{12}CO or ^{13}CO) is always much more massive than the the average molecule in molecular gas, the observed linewidth must be corrected by applying Fuller and Myer's (1992) formula:

$$\Delta v_{\text{tot}}^2 = \Delta v_{\text{obs}}^2 + 8 \ln(2) kT \left(\frac{1}{\bar{m}} - \frac{1}{m_{\text{obs}}} \right), \quad (41)$$

where m_{obs} is the mass of the emitting species, \bar{m} is the mean mass of molecular gas, and T is the kinetic temperature of the gas. For a normal helium abundance $Y = 0.28$, $\bar{m} = 2.33$. We have assumed a temperature of 20 K for the gas; the exact temperature chosen makes only a small difference in Δv_{tot} since the turbulent component of the linewidth always dominates on any scale larger than a small core. The velocity dispersion may be obtained from equation 41 by

$$\sigma = \frac{\Delta v_{\text{tot}}}{\sqrt{8 \ln 2}}. \quad (42)$$

We identify σ with $\langle \sigma^2 \rangle^{1/2}$ as defined by equation 13, since this velocity dispersion is obtained from an average linewidth for the entire cloud. With $\langle \sigma^2 \rangle$ known, we compute m_{vir} from equation 22, which directly gives us m/m_{vir} . Obtaining the average radius R_S directly from maps, and hence the cross-sectional area \mathcal{V} , the average density and internal pressure are then easily obtained using equations 12 and 13.

All that remains to deduce $\mathcal{M}/|\mathcal{W}|$ from equation 14 is

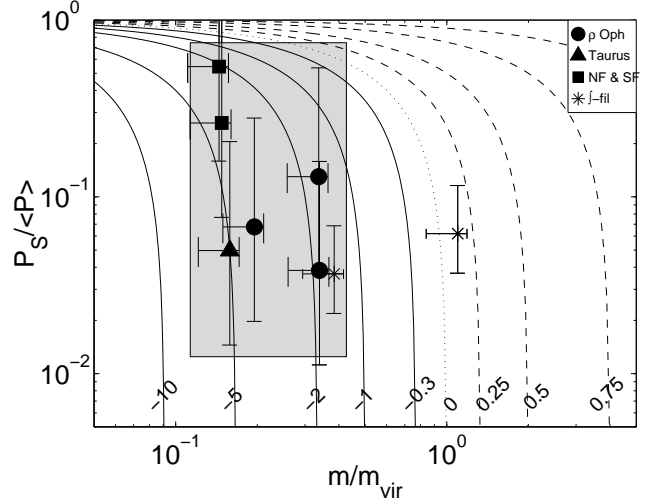


Figure 2. Helical field models are compared with the observed properties of real filaments. Curves are shown for various values of the virial parameter $\mathcal{M}/|\mathcal{W}|$. Positive values, corresponding to the dashed curves, indicate that the poloidal field is dominant, while negative values, corresponding to solid curves, indicate that the toroidal field is dominant. The dotted line represents all solutions that are neutrally affected by the helical field (including the unmagnetized solution). The \mathcal{J} -shaped filament appears twice, because we have used two independent data sets in our analysis.

to estimate the external pressure. Most of the filamentary clouds in our sample are surrounded by atomic gas. Therefore, we conservatively assume the total external pressure to be in the range $10^4 - 10^5 \text{ K cm}^{-3}$, as discussed in Section 2.3. In fact, the only exception is the \mathcal{J} -shaped filament of Orion A, which is deeply embedded in *molecular* gas. In this case, we have estimated the external pressure from measurements of the density and linewidth in the Orion A cloud (See table 2.7 for references).

Figure 2 demonstrates that most filamentary clouds reside in a part of parameter space where

$$\begin{aligned} 0.11 &\lesssim m/m_{\text{vir}} \lesssim 0.43 \\ 0.012 &\lesssim P_S/\langle P \rangle \lesssim 0.75, \end{aligned} \quad (43)$$

which is indicated by the shaded box in Figure 2. Thus, we find that filamentary clouds range considerably in their virial parameters. *However, it is remarkable that most of the clouds in our small data set appear to reside in the part of the diagram where $\mathcal{M}/|\mathcal{W}| < 0$. Thus, our virial analysis infers that the magnetic field in at least several filamentary clouds is probably helical and toroidally dominated.* We interpret this result in terms of the discussion in Section 2.5: gravity and surface pressure alone appear to be insufficient to radially bind the clouds in our sample. While this means that filaments must be quite weakly bound by gravity, we note that similar results have also been obtained by Loren (1989b) and BM92.

It is natural to wonder to what extent these conclusions could be affected by uncertainties in the observational results. The dominant sources of uncertainty in Figure 2 are probably the uncertainties in mass per unit length surface pressures. However, we have assumed very conservative

Cloud	Region	M (M_{\odot})	L (pc)	R_S (pc)	σ (km s^{-1})	Ref.	Notes
L1709	Rho Oph	140	3.6	0.23	0.479	2	1
L1755		171	6.3	0.152	0.526	2	1
L1712-29		219	4.5	0.156	0.534	2	1
DL 2 ^a	Taurus	600	6.4	0.5	1.08	4	4
\int -fil. ^b	Orion	5×10^3	13	0.25	1.41	1	2,3
		—	—	0.35	1.13	5	
NF ^c		1.55×10^4	87.3	2.25	1.54	3	1
SF ^d		3.65×10^4	300	2.25	1.29	3	1

^a Dark lane in Taurus including B18. See Mizuno et al (1995) for a more detailed map.

^b The \int -shaped filament in Orion A.

^c Northern filament in Orion (See reference).

^d Southern filament in Orion (See reference).

Table 2. We have compiled data on filamentary molecular clouds from several sources.

References: 1. Bally (1987), 2. Loren (1989), 3. Maddalena (1986), 4. Murphy and Myers (1985), 5. Tatematsu et al. (1993)

Notes 1. Little star formation. 2. Dense cores, star formation. 3. Deeply embedded in Orion A cloud. 4. Associated stars.

Cloud	m ($M_{\odot} \text{pc}^{-1}$)	m_{vir} ($M_{\odot} \text{pc}^{-1}$)	m/m_{vir}	$\langle P \rangle$ (10^4 K cm^{-3})	P_S (10^4 K cm^{-3})	$P_S/\langle P \rangle$
L1709	35.9	107	0.34	24.3	3.2	0.13
L1755	25.1	129	0.20	46.8	3.2	0.068
L1712-L29	45	132	0.34	82.4	3.2	0.038
DL 2	86.6	547	0.16	63.6	3.2	0.050
\int -fil.	355	925	0.38	1.77×10^3	64.8 ^a	0.037
	647	590	1.1	1.05×10^3	64.8	0.062
NF	164	1.11×10^3	0.15	12.1	3.2	0.26
SF	112	777	0.15	5.8	3.2	0.55

^a Determined from Bally’s (1987) density estimate and the ^{12}CO linewidth given by Maddalena (1986).

Table 3. We have reduced the data of table 2 to obtain m/m_{vir} and $P_S/\langle P \rangle$ for each filament. We assume an external pressure P_S of $10^{4.5 \pm 0.5} \text{ K cm}^{-3}$ for all filaments except the \int -shaped filament of Orion A, which is deeply embedded in molecular gas. We also assume that all filaments are oriented within 45° relative to the plane of the sky. *We only give central values in the table, but the corresponding error bars are shown in figure 2.*

ranges for the surface pressures and inclination angles of the clouds. Therefore, we do not believe that observational uncertainties can account for the helical fields that are required by our virial analysis. We also note that a more detailed model including rotation of the filament would necessarily lead to the same conclusion of a helical field. Since rotation would tend to support the cloud against gravity, even stronger toroidal fields would be required to confine the gas.

3 EXACT MHD MODELS OF FILAMENTARY STRUCTURE

The virial treatment of the previous section is perhaps the simplest and most illuminating way to understand the physics and global properties of filamentary molecular clouds. While the virial equations 4 and 18 are convenient to use, and are in fact exact expressions of magnetohydrostatic equilibrium, the analysis can say nothing of the inter-

nal *structure* of the clouds. This is the advantage of the exact analytic and numerical models developed in this section.

3.1 General Equations for Magnetized Filamentary Molecular Clouds

As in the previous section, we consider the equilibrium structure of a non-rotating, self-gravitating molecular cloud with a helical field of constant flux to mass ratios Γ_z and Γ_ϕ . We consider two equations of state for the gas: 1) the “isothermal” equation of state $P = \sigma^2 \rho$ where σ is the total velocity dispersion and 2) the “pure logatropes” of MP96 given by $P/P_c = 1 + A \ln(\rho/\rho_c)$, where P_c and ρ_c are the central (along the filament axis) pressures and densities, and A is a constant. MP96 find $A \simeq 0.2$ for molecular cloud cores. Although their analysis was based only on cloud core data, we shall assume that the same value of A might apply to filamentary clouds as well. By using these two equations of state, our analysis probably brackets the true underlying equation of state for molecular clouds; MHD cloud tur-

bulence probably results in an EOS softer than isothermal (MP96; Gehman et al. 1996), while the pure logatropes is the softest EOS to appear in the literature.

It is convenient to work in dimensionless units where density and pressure are scaled by their central values ρ_c and P_c . We further define the central velocity dispersion by

$$\sigma_c^2 = \frac{P_c}{\rho_c}. \quad (44)$$

A natural radial scale is then given by

$$r_0^2 = \frac{\sigma_c^2}{4\pi G \rho_c}, \quad (45)$$

which defines the effective core radius of the filament. Finally, we may define natural scales for the mass per unit length and magnetic field:

$$\begin{aligned} m_0 &= r_0^2 \rho_c = \frac{\sigma_c^2}{4\pi G} \\ B_0 &= P_c^{1/2}. \end{aligned} \quad (46)$$

Thus, all quantities are written in dimensionless form as follows:

$$\begin{aligned} \tilde{r} &= r/r_0 \\ \tilde{\rho} &= \rho/\rho_c \\ \tilde{m} &= m/m_0 \\ \tilde{P} &= P/P_c \\ \tilde{\sigma} &= \sigma/\sigma_c \\ \tilde{\Phi} &= \Phi/\sigma_c^2 \\ \tilde{B}_z &= B_z/B_0 \\ \tilde{B}_\phi &= B_\phi/B_0 \end{aligned} \quad (47)$$

Hereafter, we will only ever refer to Γ_z and Γ_ϕ in their dimensionless forms:

$$\begin{aligned} \tilde{\Gamma}_z &= \sqrt{\frac{\rho_c}{\sigma_c^2}} \left(\frac{B_z}{\rho} \right) \\ \tilde{\Gamma}_\phi &= \frac{1}{\sqrt{4\pi G}} \left(\frac{B_\phi}{r\rho} \right) \end{aligned} \quad (48)$$

For brevity, we will drop the tildes for the remainder of this section and the next (except for where ambiguity would result); all quantities hereafter are understood to be written in dimensionless form unless otherwise stated.

Our basic *dimensionless* equations are those of Poisson

$$\frac{1}{r} \frac{d}{dr} \left(r \frac{d}{dr} \Phi \right) = \rho \quad (49)$$

and magnetohydrostatic equilibrium

$$\frac{d}{dr} (P + P_{mag}) + \rho \frac{d}{dr} \Phi + \frac{1}{r^2} \frac{d}{dr} b_\phi, \quad (50)$$

where we have defined the magnetic pressure of the poloidal field P_{mag} as in equation 12, and a useful quantity b_ϕ that depends on the toroidal field:

$$\begin{aligned} P_{mag} &= B_z^2/(8\pi) \\ b_\phi &= r^2 B_\phi^2/(8\pi). \end{aligned} \quad (51)$$

Defining the effective enthalpy of the turbulent gas by

$$dh = \frac{dP}{\rho}, \quad (52)$$

and introducing the magnetic potentials f_z and f_ϕ

$$\begin{aligned} df_z &= \frac{dP_{mag}}{\rho} \\ df_\phi &= \frac{db_\phi}{r^2 \rho}, \end{aligned} \quad (53)$$

we may write equation 50 as

$$\frac{d}{dr} (h + \Phi + f_z + f_\phi) = 0. \quad (54)$$

We are free to specify boundary conditions for each of these potentials along the filament axis; $h = \Phi = f_z = f_\phi = 0$ at $r = 0$. Thus, equation 54 can be integrated:

$$h + \Phi + f_z + f_\phi = 0. \quad (55)$$

It is useful to define a new radial variable by the transformation

$$s = \ln(r/\alpha), \quad (56)$$

where α is a constant that is necessary only to derive a special analytic solution in Section 3.2.1. Under this transformation, equations 49 and 54 can be combined to give

$$\frac{d^2}{ds^2} (h + f_z + f_\phi) = -\Psi, \quad (57)$$

where

$$\Psi = r^2 \rho = \alpha^2 e^{2s} \rho. \quad (58)$$

To solve the differential equation 57, we must first express h , f_z , and f_ϕ in terms of s and the new quantity Ψ . Applying equation 52 to the isothermal and logatropic equations of state and integrating, we obtain the following formulas for the enthalpies:

$$\begin{aligned} h_{iso} &= \ln \rho = \ln \Psi - 2 \ln \alpha - 2s. \\ h_{log} &= A \left(1 + \frac{1}{\rho} \right) = A \left(1 + \alpha^2 e^{2s} \Psi^{-1} \right). \end{aligned} \quad (59)$$

We have also used the definitions of s (equation 56) and Ψ (equation 58) to write the final forms of the enthalpies in terms of these variables.

Assuming constant flux to mass ratios Γ_z and Γ_ϕ we derive from equations 31, 32, and 51

$$\begin{aligned} P_{mag} &= \frac{\Gamma_z^2 \rho^2}{8\pi} = \frac{\Gamma_z^2 \Psi^2}{8\pi \alpha^4 e^{4s}} \\ b_\phi &= \frac{\Gamma_\phi^2 \Psi^2}{8\pi}. \end{aligned} \quad (60)$$

Substituting these relations into equations 53 and integrating, we obtain

$$\begin{aligned} f_z &= \frac{\Gamma_z^2}{4\pi} (\rho - 1) = \frac{\Gamma_z^2}{4\pi} \left(\frac{\Psi}{\alpha^2 e^{2s}} - 1 \right) \\ f_\phi &= \frac{\Gamma_\phi^2}{4\pi} \Psi, \end{aligned} \quad (61)$$

where we have applied our boundary conditions that both f_z and f_ϕ vanish along the axis of the filament where $\rho = \rho_c$ and $\Psi = 0$. We have expressed all quantities in equations 59 and 61 in terms of s and Ψ alone. Thus, equation 57 is closed and can, at least in principle, be solved for Ψ . Since ρ , P_{mag} , and b_ϕ are written in terms of Ψ (equations 58 and 60), these quantities may be determined. Finally, the poloidal and toroidal magnetic fields may be obtained from equations 51.

3.2 Analytic Solutions

Before discussing the numerical solution of equation 57, we derive a few special solutions that can be expressed in closed analytic form. Specifically, we give a brief derivation of the unmagnetized isothermal solution that was found by Ostriker (1964), and demonstrate that it exactly obeys our virial equation 18. We note that this solution is a special case of a more general magnetized solution obtained by Stodólkiewicz (1963); for brevity, we shall refer to this solution as the Ostriker solution for the remainder of this paper. We also find a singular solution for logatropic filaments. It is unlikely that either of these special solutions describe real filaments, which are probably magnetized and non-singular, but they do serve as important benchmark results to compare with our more elaborate magnetized models.

3.2.1 The Ostriker Solution: Unmagnetized Isothermal Filaments

The analytic solution for the special case of an unmagnetized isothermal filament is easily obtained using the mathematical framework of the previous section. Using the definition of h_{iso} (from equation 59) in equation 57, we easily obtain

$$\frac{d^2}{ds^2} (\ln \Psi) = -\Psi. \quad (62)$$

This equation can be solved in closed form; the solution is simply

$$\Psi = 2 \operatorname{sech}^2 s. \quad (63)$$

Converting back to r and ρ , the equation takes the form

$$\rho = \frac{8/\alpha^2}{(1 + r^2/\alpha^2)^2}. \quad (64)$$

The boundary condition at $r = 0$ is $\rho = 1$ in our dimensionless units; therefore, we require that $\alpha = \sqrt{8}$, giving the final density structure for the Ostriker solution:

$$\rho = \frac{\rho_c}{(1 + r^2/8r_0^2)^2}, \quad (65)$$

where we have restored the dimensional units. We note that the density decreases as $\sim r^{-4}$ at large radii. That such steep density profiles have not been observed could be explained by three possibilities: 1) molecular clouds are not isothermal. A softer EOS would give a less steeply falling density at large radius; 2) real clouds contain dynamically important magnetic fields that modify the structure of the filament at large radius; 3) real filaments are always truncated by external pressure. If the filament is truncated before the $\sim r^{-4}$ envelope is reached, such steep behaviour would not be observed. We demonstrate in Section 4.1.2 that either of possibilities 1) or 2) can explain the observed properties of molecular clouds.

It is simple to verify the virial equation 21 for the Ostriker solution 65. Integrating the density of the Ostriker solution, we obtain the mass per unit length interior to radius r :

$$\begin{aligned} m(r) &= \frac{m_{vir}}{1 + 8(r_0/r)^2} \\ &= \frac{\pi r^2 \rho_c}{1 + r^2/8r_0^2}. \end{aligned} \quad (66)$$

Now suppose that we truncate the filament at radius R_S where the pressure in the filament falls to that of the external medium P_S . Then the ratio of surface pressure P_S to average pressure internal to R_S can be expressed as

$$\frac{P_S}{\langle P \rangle} = \frac{\rho_S}{\langle \rho \rangle} = \frac{\pi R_S^2 \rho_S}{m}. \quad (67)$$

Substituting equations 65 and 66 into equation 67, we easily obtain

$$\frac{P_S}{\langle P \rangle} = \frac{1}{1 + R_S^2/8r_0^2}. \quad (68)$$

Rearranging equation 66, we write the radius R_S as a function of the mass per unit length internal to that radius:

$$\frac{R_S^2}{r_0^2} = \frac{8}{(m_{vir}/m - 1)}. \quad (69)$$

Substituting this result into equation 68 and simplifying, we obtain

$$\frac{P_S}{\langle P \rangle} = 1 - \frac{m}{m_{vir}} \quad (70)$$

which is identical to our virial equation 21 for an unmagnetized isothermal filament. Thus, we have shown that the Ostriker solution exactly obeys our virial equation, as all filamentary equilibria must.

3.2.2 Singular Logatropic Filaments

Although we have been unable to find the analogue of the Ostriker solution for the logatropic EOS, we have been successful in finding a singular solution. For this model, we reinterpret ρ_c as the density at some fiducial radius. Substituting the enthalpy of the logatropic gas (from equation 59) into equation 55, we easily obtain the gravitational potential:

$$\Phi = -A(1 + \rho^{-1}). \quad (71)$$

With the help of this expression, Poisson's equation 49 becomes

$$\frac{A}{r} \frac{d}{dr} \left(r \frac{d}{dr} \rho^{-1} \right) = \rho. \quad (72)$$

Now we postulate a power law solution of the form

$$\rho = cr^\alpha, \quad (73)$$

and find that a solution can only be obtained if $c = \sqrt{A}$. Thus, the final solution with dimensional units restored is

$$\frac{\rho}{\rho_c} = \sqrt{A} \left(\frac{r}{r_0} \right)^{-1}. \quad (74)$$

It is useful to compare our solution with the singular logatropic *sphere* found by MP96:

$$\frac{\rho_{sphere}}{\rho_c} = \sqrt{2A} \left(\frac{r}{r_0} \right)^{-1}, \quad (75)$$

where we have rewritten their solution using our definition of r_0 . (Their definition of r_0 differs from ours by a factor of 3. Our definition is the customary choice for filaments.). It is remarkable that both singular logatropic spheres and filaments obey precisely the same power law.

3.3 Bonner-Ebert Stability of Magnetized Filament: Analytic Results

We have addressed the Bonnor-Ebert stability of *uniform* magnetized filaments in Section 2.6. In that section, we presented a physical argument based on the virial theorem to show that uniform magnetized filaments with helical fields are always stable in the sense of Bonnor and Ebert. In this section, we extend that argument to *general* magnetized filamentary equilibria using the mathematical framework of Section 3.1.

Again we consider a radial perturbation of a filamentary cloud in which the mass per unit length m is conserved. Following MP96, we shall also require that the central velocity dispersion σ_c remain unchanged. Referring to equations 46 and 48, we may write

$$\tilde{m} = \frac{m}{m_0} = \frac{4\pi G m}{\sigma_c^2}. \quad (76)$$

Thus, we see that the dimensionless mass per unit length \tilde{m} is also conserved during the perturbation. Since \tilde{m} is implicitly a function of \tilde{r} alone, the dimensionless radius \tilde{R}_S must remain fixed during the perturbation. Therefore, we find that the radial perturbation takes the form of a simple rescaling of the dimensionless solution with *none* of the dimensionless variables perturbed whatsoever. With this result in hand, we write

$$\begin{aligned} P_S &= P_c \tilde{P}_S = \sigma_c^2 \rho_c \tilde{P}_S \\ R_S &= \sqrt{\frac{\sigma_c^2}{4\pi G}} \rho_c^{-1/2} \tilde{R}_S, \end{aligned} \quad (77)$$

where σ_c , \tilde{P}_S , and \tilde{R}_S all remain fixed during the perturbation. Eliminating ρ_c , we obtain the result

$$R_S = \sqrt{\frac{\sigma_c^4}{4\pi G}} (\tilde{P}_S \tilde{R}_S^2)^{1/2} P_S^{-1/2}. \quad (78)$$

Since $R_S \propto P_S^{-1/2}$, we find that

$$\frac{dR_S}{dP_S} < 0 \quad (79)$$

for *all* external pressures P_S . Therefore, we conclude that all self-gravitating filaments that are initially in a state of equilibrium (which requires $m \leq m_{mag}$ by equation 23), are stable in the sense of Bonner and Ebert.

4 NUMERICAL SOLUTIONS

We now turn our attention to numerical solutions of equation 57 with arbitrary helical magnetic field. While the second order differential equation 57 is most useful for the analytic solutions of the previous section, it is most convenient for numerical solutions to write it as a pair of first order equations. This is best accomplished by writing the gravitational acceleration as

$$g = -\frac{d}{dr}\Phi = -\frac{1}{r}\frac{d}{ds}\Phi. \quad (80)$$

Then Poisson's equation 49 becomes

$$\frac{1}{r^2}\frac{d}{ds}(rg) = -\rho. \quad (81)$$

	H_1	H_2
Isothermal	-2	Ψ^{-1}
Logatropic	$-2Ae^{2s}\Psi^{-1}$	$Ae^{2s}\Psi^{-2}$

Table 4. H_1 and H_2 are the functions related to the enthalpy by equation 84.

Note that there is no reason for numerical solutions to retain the constant scale factor α introduced in equation 56. For the remainder of this section, we will take $\alpha = 1$. With the help of equation 55 and the definition of Ψ (equation 58), our numerical system becomes

$$\begin{aligned} \frac{d}{ds}(h + f_z + f_\phi) &= rg \\ \frac{d}{ds}(rg) &= -\Psi. \end{aligned} \quad (82)$$

It was shown in Section 3.1 that h , f_z , and f_ϕ have been written as functions of Ψ ; thus, equations 82 can be rewritten as differential equations for Ψ and g . We write these equations explicitly below.

Denoting the derivative $\frac{d}{ds}$ with a prime ($'$), we derive from equations 53

$$\begin{aligned} f'_z &= \frac{\Gamma_z^2}{4\pi} e^{-2s} (\Psi' - 2\Psi) \\ f'_\phi &= \frac{\Gamma_\phi^2}{4\pi} \Psi'. \end{aligned} \quad (83)$$

Using equations 59, we must calculate h' separately for the isothermal and logatropic equations of state. We note that h' can be written in the general form

$$h' = H_1(s, \Psi) + H_2(s, \Psi)\Psi', \quad (84)$$

where the functions H_1 and H_2 are given in table 4.

Using equations 83 and 84, we express our system of equations 82 in its final form:

$$\begin{aligned} \Psi' &= \frac{rg - H_1 + \frac{\Gamma_z^2}{2\pi} e^{-2s} \Psi}{H_2 + \frac{\Gamma_\phi^2}{4\pi} + \frac{\Gamma_z^2}{4\pi} e^{-2s}} \\ g' &= -(g + e^{-s}\Psi). \end{aligned} \quad (85)$$

Since H_2 is positive definite, this dynamical system is regular on the entire interval $s \in (-\infty, \infty)$.

These equations are now in a form that can be numerically integrated given appropriate initial conditions at the axis of the filament ($r = 0$). The problem arises however that $r = 0$ occurs at $s = -\infty$ in our transformed variable; thus, we start the integration at a small but finite value of r . We expect that ρ tends to a constant value of unity near the axis for any non-singular distribution. From the definition of Ψ (equation 58), we find that $\Psi_0 \approx e^{s_0}$ where s_0 is the initial value chosen for s (typically ≈ -10). Recalling that g is the gravitational acceleration, we apply Gauss's law to find the initial value for g :

$$g_0 = -\frac{r}{2} = -\frac{1}{2}e^{s_0}. \quad (86)$$

The numerical integration is now straightforward and may be performed by any standard method. We note that a solution is entirely determined by the choice of three free pa-

rameters: Γ_ϕ , Γ_z , and the (dimensionless) radius of pressure truncation R_S .

4.1 Numerical Results

We have used a standard Runge-Kutta method to numerically integrate equations 85 for the isothermal EOS and the logatropes. We have shown in Section 2.7 that many filamentary clouds are probably wrapped by helical magnetic fields. However, before considering the most general case of helical fields in Section 4.1.2, we first separately consider the effects of poloidal and toroidal magnetic fields in Section 4.1.1. We note that purely poloidal fields are not allowed by our virial analysis, and purely toroidal fields are probably unrealistic. Nevertheless, this is the best way to understand the roles of each field component in our more general helical field models.

4.1.1 Models With Purely Poloidal and Toroidal Fields

Since any magnetized solution is characterized by two parameters Γ_z and Γ_ϕ , it is most useful to consider separately the effects of the poloidal and toroidal fields before considering more general helical field configurations. Figures 3 and 4 show the density and pressure profiles, the magnetic structure, and the mass per unit length for the isothermal and logatropic equations of state. We have also included the velocity dispersion and average velocity dispersion (given by equation 13) for the logatropic equation of state.

On each set of figures we have shown the density, pressure, and velocity dispersion structure of the unmagnetized solutions with dashed lines. For isothermal solutions, we have also drawn a line representing the asymptotic r^{-4} behaviour of the Ostriker solution. Similarly, the r^{-1} singular solution has been included on density profiles for logatropic filaments. These power laws are meant as a guide in interpreting the asymptotic behavior of the solutions; we find that they are obeyed at large radius for all unmagnetized filaments.

The solutions are shown out to large radius but may be truncated by the following procedure. Given an external pressure P_S , the radius at which the pressure inside the filament equals P_S may be read from the pressure graphs. This defines the radius of pressure truncation. Only the part of the solution that is internal to this radius is relevant.

Comparing the unmagnetized solutions (dashed lines) in Figures 3 and 4, we observe that the density profile of the unmagnetized logatropic filament is slightly more centrally concentrated than the isothermal Ostriker solution, but falls off much less steeply at large radius. These figures also show that isothermal and logatropic filaments both tend to finite mass per unit length, although they differ in that isothermal filaments approach the critical mass per unit length only asymptotically as their radii tend to infinity. As discussed in Section 2, this limit represents the critical mass per unit length m_h (see equation 22) beyond which no equilibrium is possible. For the isothermal filament, we find both analytically (equation 66) and numerically that $m_h = 8\pi m_0$, where m_0 is the mass scale defined by equation 46. For the unmagnetized logatropic filament, we find numerically that $m_h = 185.8m_0$. Logatropic filaments can support a greater

mass per unit length for equivalent central velocity dispersion σ_c . This is easily understood since the *average* velocity dispersion $\langle\sigma^2\rangle^{1/2}$ always exceeds the central value offering more turbulent support to the filament.

Perhaps the most notable feature of logatropic filaments is that they “self-truncate” at finite radius and density $\rho = \rho_c \exp(-1/A)$ where the velocity dispersion and pressure vanish. The logatropic EOS is designed to have a nearly isothermal core and a rising velocity dispersion outside of the core radius. At some point, however, the velocity dispersion turns over and falls to zero. The velocity dispersion could of course never vanish in a real cloud since all real clouds are truncated by finite external pressure. Whether the region of outwardly falling velocity dispersion actually falls within the pressure truncation radius in fits to real clouds is addressed in Section 4.2, where we attempt to constrain our models using the observational results of table 2.7.

Because of the way in which we have defined Γ_z (equation 31), B_z is exactly proportional to the density. The toroidal field, however, shows a more interesting structure; B_ϕ always vanishes along the axis of the filament, as it must for the field to be continuous across the axis. We note that the logarithmic radial scale of Figure 4 makes the vanishing of B_ϕ at the axis difficult to see in some cases. It also is found to decay at large radius for isothermal filaments since $B_\phi = \Gamma_\phi r \rho \propto r^{-3}$. Hence, there is a single maximum in the toroidal field structure. For logatropic filaments, the r^{-1} asymptotic behaviour of the density implies that $B_\phi = \Gamma_\phi r \rho$ tends to a constant value at large radius. Thus, the toroidal field in logatropic filaments lacks the local maximum found for isothermal filaments.

The effects of poloidal and toroidal magnetic fields on the density structure are apparent in Figures 3 and 4. For either EOS, the poloidal magnetic field supports the cloud and causes it to be more extended radially than the corresponding unmagnetized filament. Toroidal magnetic fields, on the other hand, pinch the filament to smaller radial extent. Thus, we find our numerical results to be in agreement with the results of our virial analysis in Section 2.

It is significant that purely poloidal fields always steepen the outer density profile, while toroidal fields make it more shallow. For isothermal filaments, poloidal fields always result in density profiles that are steeper than the r^{-4} behaviour of the Ostriker solution; this is true of even logatropic filaments when the field is of sufficient strength. These steep density profiles have never been observed, so purely poloidal fields do not match the data. Thus, it seems likely that the field must have a toroidal component if a realistic density profile is to be achieved.

We find that the magnetic field has a *dramatic* effect on the critical mass per unit length m_{mag} of the cloud. For either EOS, a poloidal magnetic field increases m_{mag} , since the poloidal field acts to support the cloud against self-gravity. The toroidal magnetic field works with gravity, thus decreasing the maximum mass per unit length that can be supported. These conclusions are in agreement with our virial results from Section 2.

From Figures 3 and 4, we note that all isothermal filaments that are unmagnetized or contain a purely toroidal field tend to the same mass per unit length m_h . This is easily explained by our virial equation 18 since the toroidal field always tends to zero at large radius for isothermal filaments.

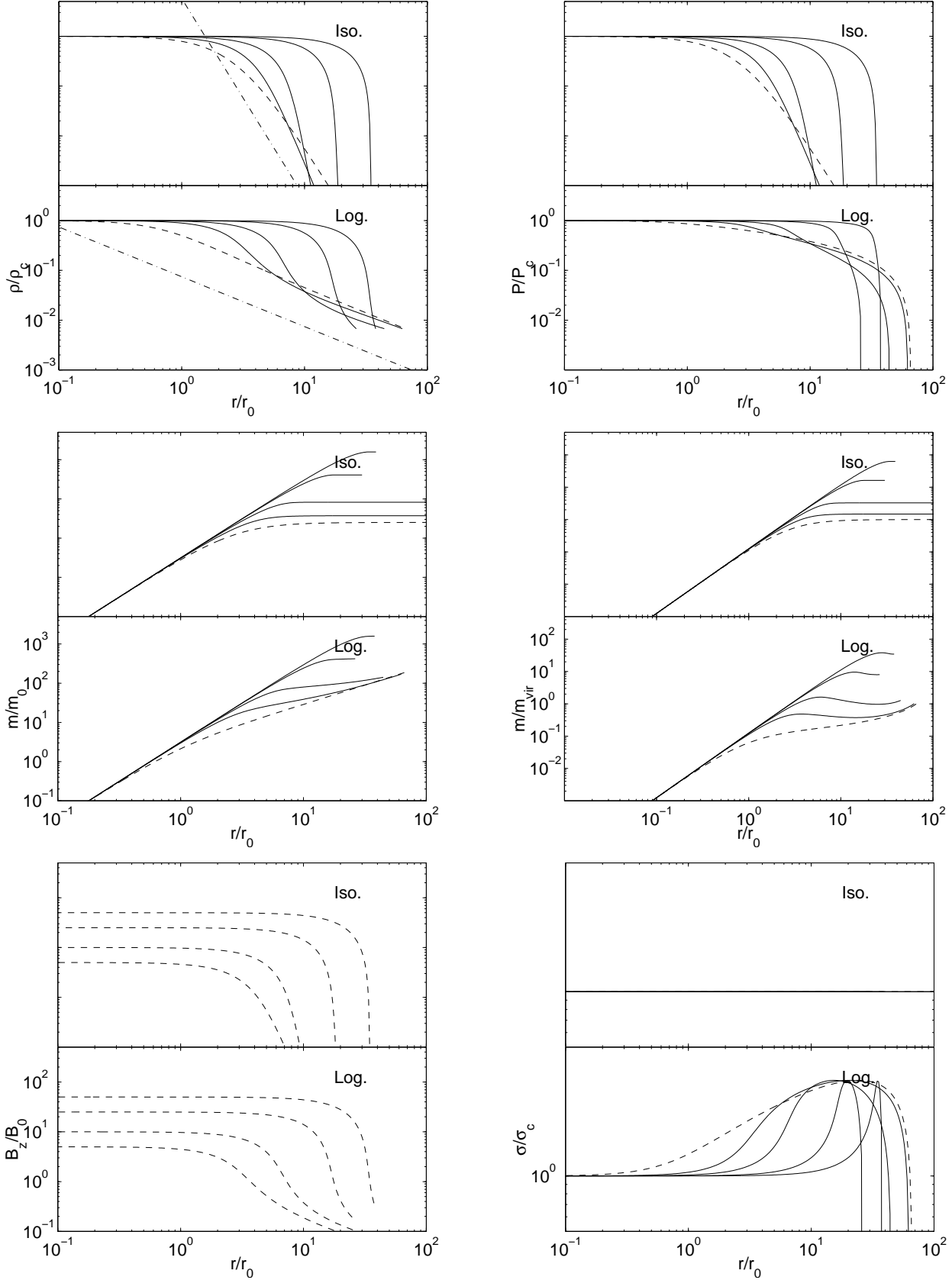


Figure 3. Isothermal and logatropic filaments with purely poloidal magnetic field: $\Gamma_z = 0$ (dashed line), 5, 10, 25 and 50. The dot-dashed lines represent the r^{-4} density structure of the Ostriker solution at large radius and the r^{-1} behaviour of the singular logatropic solution.

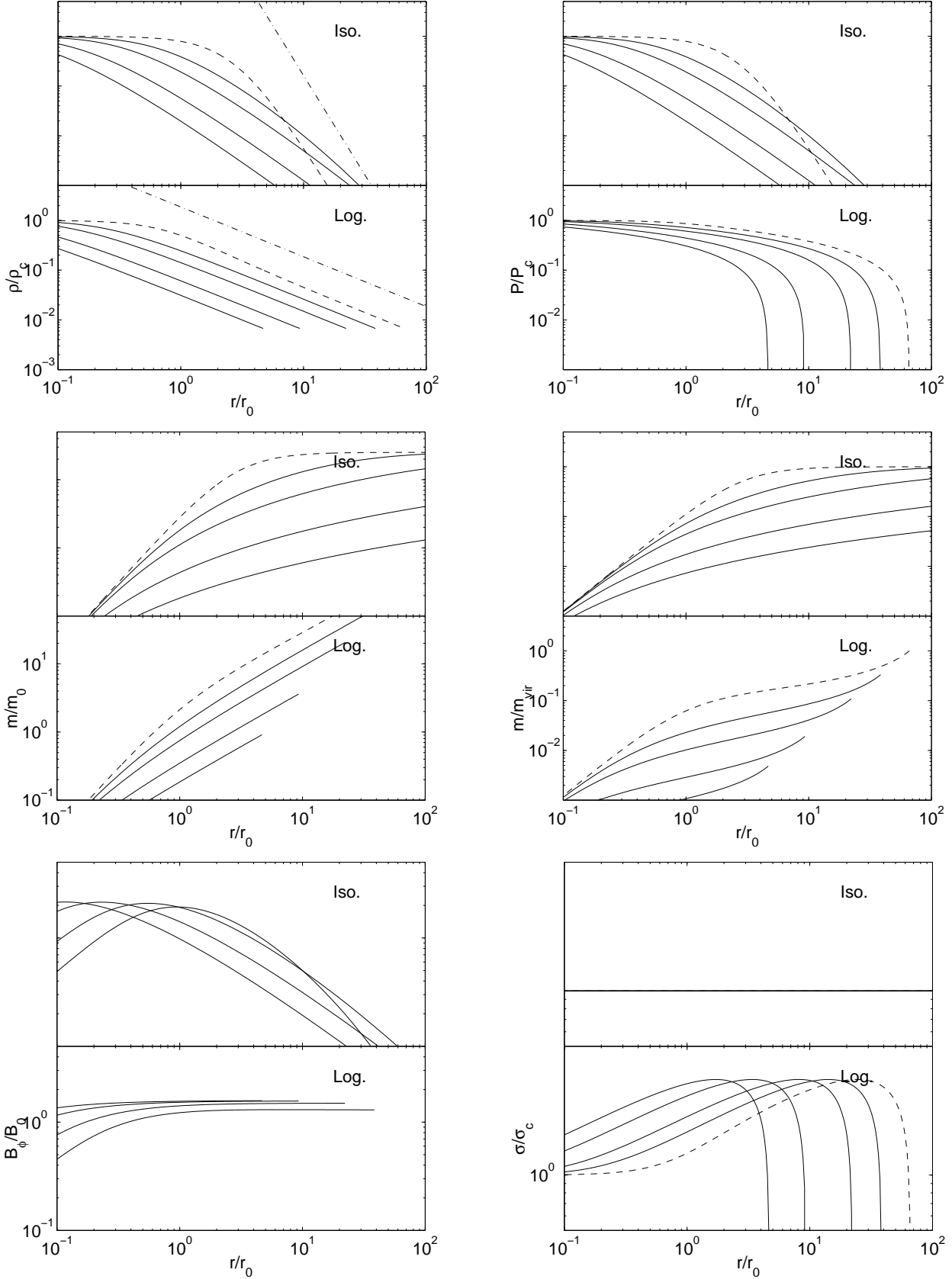


Figure 4. Isothermal and logatropic filaments with purely toroidal magnetic field: $\Gamma_\phi = 0$ (dashed line), 5, 10, 25 and 50. The dot-dashed lines have the same meaning as in Figure 3.

The critical mass per unit length m_{mag} clearly cannot be affected, since the toroidal field only enters the virial equation through its surface value. This is *not* the case for logatropic filaments because B_ϕ tends to a constant value at large radius.

4.1.2 Helical Field Models

In Section 2.7, we provided evidence based on our virial analysis that filamentary clouds likely contain toroidally dominated helical magnetic fields. At this point, we shall take a further step by comparing our exact MHD models with the observed properties of filamentary molecular clouds. As we have noted in Section 4, a numerical solution is completely determined by the choice of three dimensionless parameters; the flux to mass ratios Γ_z , Γ_ϕ , and the dimensionless radius of pressure truncation R_S/r_0 . For convenience, we replace R_S/r_0 with a new *concentration parameter* C defined as

$$C = \log_{10} \left(\frac{R_S}{r_0} \right), \quad (87)$$

where r_0 is the radial scale defined by equation 48. The concentration parameter C provides a useful description of the degree to which a filamentary cloud is centrally concentrated. We note that our definition of C is analogous to the concentration parameter $C = \log_{10}(r_t/r_0)$ defined for King models of globular clusters (See Binney & Tremaine 1987). Our concentration parameter differs only in that the tidal radius r_t is replaced by the pressure truncation radius, and our r_0 is smaller by a factor of 3. *While we use C primarily as a theoretical parameter, we note that it is, in principle observable.*

Although R_S can be observed with little difficulty, obtaining an accurate value for C is difficult because of the uncertainty in the core radius r_0 . According to equation 45, the core radius depends on both the central density and velocity dispersion along the axis of the filament, both of which might be quite uncertain. We can, however, estimate a rough upper bound to C using the data of table 2. We do not presently know whether the central (axial) velocity dispersions of filamentary clouds are dominated by non-thermal motions, as the bulk of the cloud certainly is, or if the velocity dispersions are thermal, as they are in many low-mass cloud cores. Nevertheless, we do know that σ_c must be *at least* the thermal value, which is 0.23 km s^{-1} , assuming a temperature of $15K$. Central densities are probably less than about 10^4 cm^{-3} , which is typical of a core. Therefore, equation 45 implies that r_0 is probably not less than $\approx 0.04 \text{ pc}$. In Table 2, we find that $R_S \lesssim 0.5 \text{ pc}$ for most (but not all) of the filaments in our sample. Therefore, equation 87 implies that most filamentary clouds should have concentration parameters that are less than approximately 1.1. This estimate should be treated with caution, considering the uncertainties and generalizations in our calculation. In particular, we note that larger filaments, such as the Northern and Southern Filaments in the Orion region (See Table 2) have radii that are many times larger than the value that we used in our calculation and may, therefore, have concentration parameters that exceed our upper bound.

Three observable quantities shall be required to constrain our theoretical models. We have previously (Section 2.7) found the virial parameters $P_S/\langle P \rangle$ and m/m_{vir} to be

useful in showing that toroidally dominated helical fields play an important role in the virial equilibrium of filamentary clouds. We use these parameters, as well as a third parameter specifying the ratio of average magnetic to kinetic energy densities to constrain our models. Accordingly, we define a virial parameter

$$X = \frac{M}{K}, \quad (88)$$

where M and K are the average magnetic and kinetic energy densities within the cloud defined by

$$\begin{aligned} M &= \frac{\int_V (B_z^2 + B_\phi^2) dV}{8\pi V} \\ K &= \frac{3}{2} \langle \rho \rangle \langle \sigma^2 \rangle, \end{aligned} \quad (89)$$

and V is the volume of the cloud (not to be confused with \mathcal{V}). Myers and Goodman (1988a,b) have provided considerable observational evidence that the average magnetic and kinetic energy densities are in approximate equipartition, with $M \approx K$ to within a factor of order 2. Therefore, we impose the auxiliary constraint that

$$X \approx \mathcal{O}[1] \quad (90)$$

for filamentary clouds with realistic magnetic fields. This equipartition of energy has been explained by attributing the non-thermal motions within molecular clouds to internally generated Alfvénic turbulence (BM92). Since super-Alfvénic turbulence is highly dissipative, the Alfvén speed poses a natural limit for the non-thermal velocity dispersion (BM92). Thus, we expect $\sigma \approx v_A$ for molecular clouds. Defining the average squared Alfvén speed as

$$\langle v_A^2 \rangle = \frac{\int_0^m v_A^2 dm'}{m}, \quad (91)$$

it is easy to show that

$$X = \frac{\langle v_A^2 \rangle}{3\langle \sigma^2 \rangle}. \quad (92)$$

Therefore, $X \approx 1$ is a natural result for magnetized clouds supported against gravity by Alfvénic turbulence. In the analysis that follows, we assume that

$$0.2 \leq X \leq 5 \quad (93)$$

for all reasonable models and that $0.5 \leq X \leq 2$ is appropriate for our most realistic models.

4.1.3 Monte Carlo Exploration of the Parameter Space

In this Section, we perform a Monte Carlo sampling of our parameter space in order to determine which values of Γ_z , Γ_ϕ , and C result in models that obey all of our constraints. The Monte Carlo analysis is very straightforward. We simply assign random values to the three theoretical parameters and compute helical field models using the mathematical framework of Section 3.1. Once a solution has been obtained, we compute m/m_{vir} , $P_S/\langle P \rangle$, and X using equations 15, 12, and 88, from which we easily determine whether or not the solution obeys our constraints. Figure 5 shows the results of our Monte Carlo analysis for isothermal models, while Figure 6 shows the results for logatropic models. Each point in these figures represents a model that obeys our constraints

on m/m_{vir} and $P_S/\langle P \rangle$; models that fall outside of these constraints have been discarded.

The grayscale in Figures 5a and 6a represent different ranges for X . The most likely range of X , with $0.5 \leq X \leq 2$ is shown as the lightest coloured points. The next darkest gray dots represent a less likely, but still possibly allowed range, with $0.2 \leq X \leq 5$, while the darkest gray dots represent models that are outside of these ranges, and therefore have unrealistically large or small magnetic fields. It should be noted that there is relatively little overlap between these regions; they map out quite distinct regions on the diagrams. From Figure 5a, we find that the allowed ranges for the flux to mass ratios are approximately

$$\begin{aligned} 5 &\lesssim \Gamma_\phi \lesssim 25 \\ \Gamma_z &\lesssim 8 \end{aligned} \quad (94)$$

for isothermal filaments with $0.5 \leq X \leq 2$. A somewhat larger region of the parameter space is allowed for filaments with $0.2 \leq X \leq 5$. Comparing with Figure 6a, we find that the allowed flux to mass ratios are somewhat larger for logatropic filaments, where we find

$$\begin{aligned} 10 &\lesssim \Gamma_\phi \lesssim 40 \\ 10 &\lesssim \Gamma_z \lesssim 20 \end{aligned} \quad (95)$$

when $0.5 \leq X \leq 2$. We note that Γ_z is more tightly constrained than Γ_ϕ for both isothermal and logatropic filaments.

In Figures 5b and 6b, we plot our magnetic parameter X , for the allowed models, against the poloidal flux to mass ratio Γ_z . We find that X has a very strong dependence on Γ_z for both isothermal and logatropic models. Moreover, we find that there is no obvious correlation between X and Γ_ϕ . Since we can regard X as nearly a function of Γ_z alone, the auxiliary constraint on X *directly* constrains Γ_z . It is for this reason that somewhat tighter constraints are obtained on Γ_z in equations 94 and 95, than on Γ_ϕ .

Figures 5c and 6c show the dependence of the concentration parameter C on m/m_{vir} and $P_S/\langle P \rangle$ for models that are allowed by the observations. We find that C may range from 0 to ≈ 3 for isothermal models, but $C \lesssim 1.7$ for most solutions where $0.5 \leq X \leq 2$. Moreover, we find that C correlates rather well with $P_S/\langle P \rangle$, with greater values of $P_S/\langle P \rangle$ corresponding to smaller values of C . We note that most filamentary clouds *probably* have $C \lesssim 1.1$, considering our discussion in Section 4.1.2. However, we do not enforce this upper bound as a rigid constraint, since further data on the central densities and velocity dispersions of filamentary clouds needs to be obtained in order to make our argument definitive. We find that $C \gtrsim 1$ whenever $P_S/\langle P \rangle \lesssim 0.25$; therefore, isothermal filaments with $C \lesssim 1$ must be subject to external pressures that are at least one fourth of the mean internal pressure. Such relatively high external pressures are well within the range of pressures allowed by equation 43. The concentration parameter C is much more restricted for logatropic models, where C may range only from approximately 0.4 to 1.2. As a general trend, we find that C increases with m/m_{vir} , and also as $P_S/\langle P \rangle$ decreases. This is a natural result, since filaments become more radially extended, with greater C , as they become closer to their

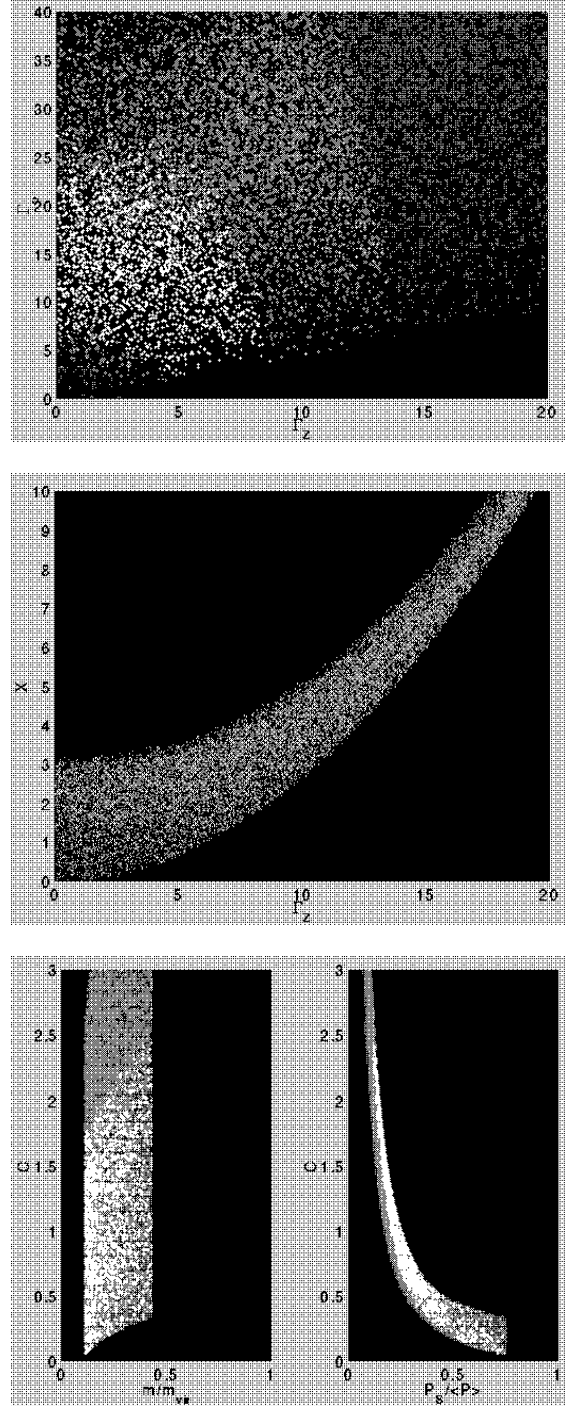


Figure 5. Isothermal Models. We show the results of our Monte Carlo analysis for isothermal filaments. Each point on these figures represents a model that obeys the observational constraints given in equation 43; thus, we determine which ranges of our theoretical parameters Γ_z , Γ_ϕ , and C result in models that agree with the available observational data. a) (top) The grayscale represents different ranges for the magnetic parameter X , as defined in equation 88. The most realistic solutions, with $0.5 \lesssim X \lesssim 2$ are shown as white dots. The intermediate gray dots represent models that are less likely, but still possibly allowed, with $0.2 \lesssim X \lesssim 5$. The dark gray dots represent models that are outside of these ranges, and therefore have unrealistic magnetic field strengths. c) (middle) We show that X is determined mainly by Γ_z . c) (bottom) We show the allowed ranges of the concentration parameter C . The shading is the same as in a). However, we note that the darkest gray dots are mostly hidden “behind” the intermediate gray, in this case.

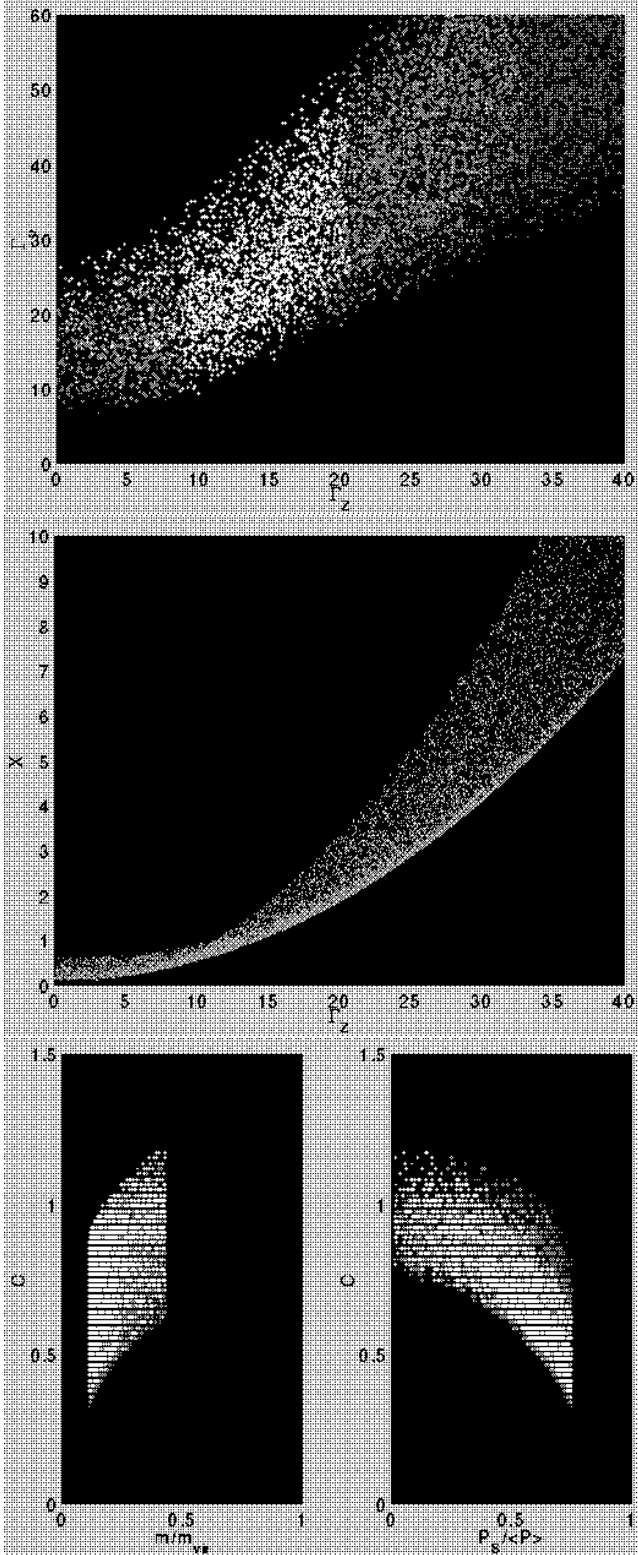


Figure 6. Logatropic Models. We show the results of our Monte Carlo analysis for logatropic filaments, as in Figure 5.

critical configurations with vanishing $P_s/\langle P \rangle$ and maximum m/m_{vir} .

4.2 “Best-Fitting” Models For Magnetized Filamentary Clouds

In Figure 7, we show 50 isothermal helical field models that span the range of parameters allowed by equations 43 and 93. We see that our allowed models possess a number of very robust characteristics. Most importantly, we find that most of our isothermal models have outer density profiles that fall off as $\sim r^{-1.8}$ to r^{-2} , with some of most truncated models having somewhat more shallow profiles. This is most clearly shown in Figure 7b, where we have plotted the power law index $\alpha = d \ln \rho / d \ln r$ as a function of the dimensionless radius r/r_0 . We observe that α becomes more negative with increasing radius, but that *none of our models ever have density profiles that are steeper than r^{-2} . Thus, we find that our isothermal helical field models have density distributions that are much more shallow than the r^{-4} Ostriker solution.* This radical departure from the Ostriker solution is clearly due to the dominance of the magnetic field over gravity in the outer regions. The overall effect of the helical field is to modify the density structure of the Ostriker solution so that a much more realistic form is obtained. In particular, we note that A98 and LAL98 have recently used extinction measurements of background starlight in the near infra-red to show that two filamentary clouds, namely L977 and IC 5146, have r^{-2} density distributions. Our helical field models have density profiles that are essentially the same as those obtained for models with purely toroidal fields in Section 4.1.1. Therefore, we conclude that the outer density distribution is shaped primarily by the toroidal component of the field. We note, however, that the toroidal field is in fact much weaker than the poloidal field throughout most of a filamentary cloud. In all cases, the basic magnetic structure is that of a poloidally dominated core region surrounded by a toroidally dominated envelope, where the field is relatively weak.

In Figure 8, we show a sample of 50 logatropic models that are allowed by our constraints. The main difference between the logatropic models and the isothermal models shown in Figure 7 is that there is a much greater variety of allowed density distributions for the logatropes. We find logatropic filaments with density profiles as shallow as r^{-1} and as steep as $r^{-1.8}$. Unlike the isothermal solutions, α does not decrease monotonically. Rather, it usually reaches a minimum value somewhat less than -1 when $r/r_0 \approx 1$ to 3, and *increases* at larger radii. The result is that the density distribution usually contains a small region where the density falls quite rapidly, which is surrounded by an envelope with a more gentle power law. Many logatropic models have density profiles that are too shallow to explain the A98 and LAL98 data. However, we have also found many logatropic models that approach the observed r^{-2} profiles. *The main difference between isothermal and logatropic models is that isothermal filaments produce a nearly “universal” $r^{-1.8}$ to r^{-2} density profile, while logatropic filaments show a much larger range of behaviour.*

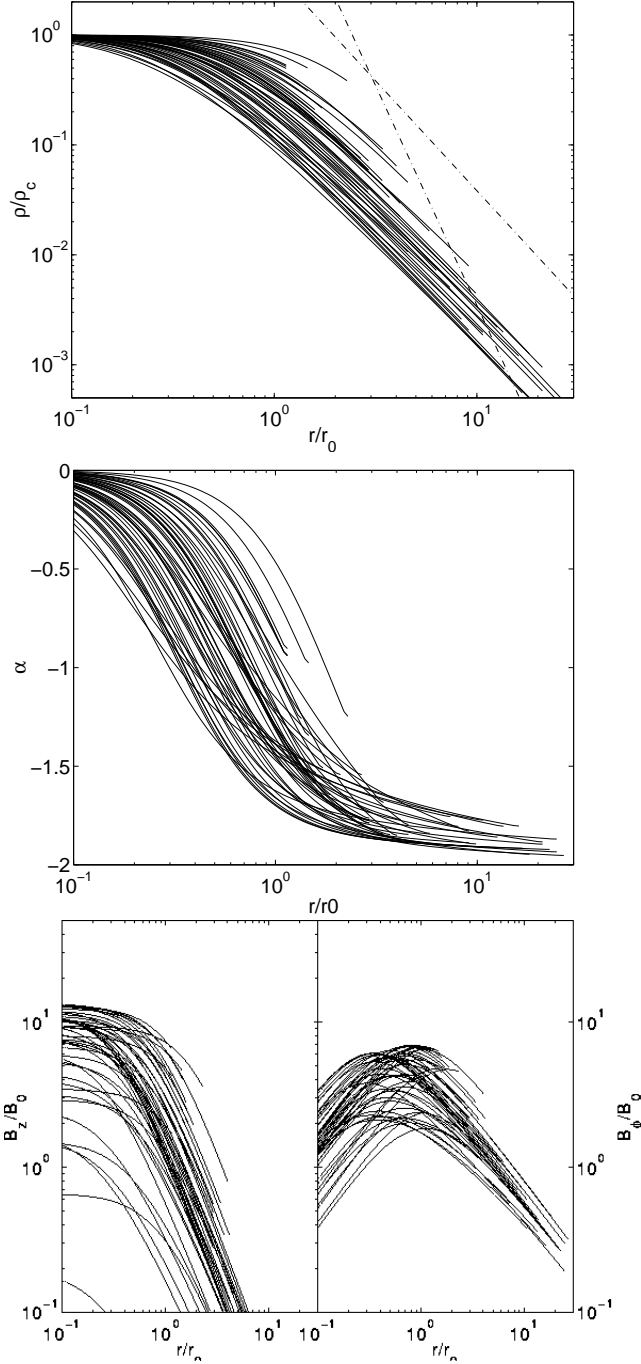


Figure 7. We show a sample of 50 isothermal models that span the range of allowed parameters given in equations 43 and 93. a) (top) We show the density profiles of the models. The dashed lines represent the r^{-4} density profile of the Ostriker solution and an r^{-2} profile, which is in agreement with the observed density profiles of filamentary clouds (Alves et al. (1998), Lada, Alves, and Lada (1998)). b) (middle) We show the how the power law index $d \ln \rho / d \ln r$ behaves with radius. c) (bottom) We show the behaviour of the poloidal and toroidal components of the magnetic field.

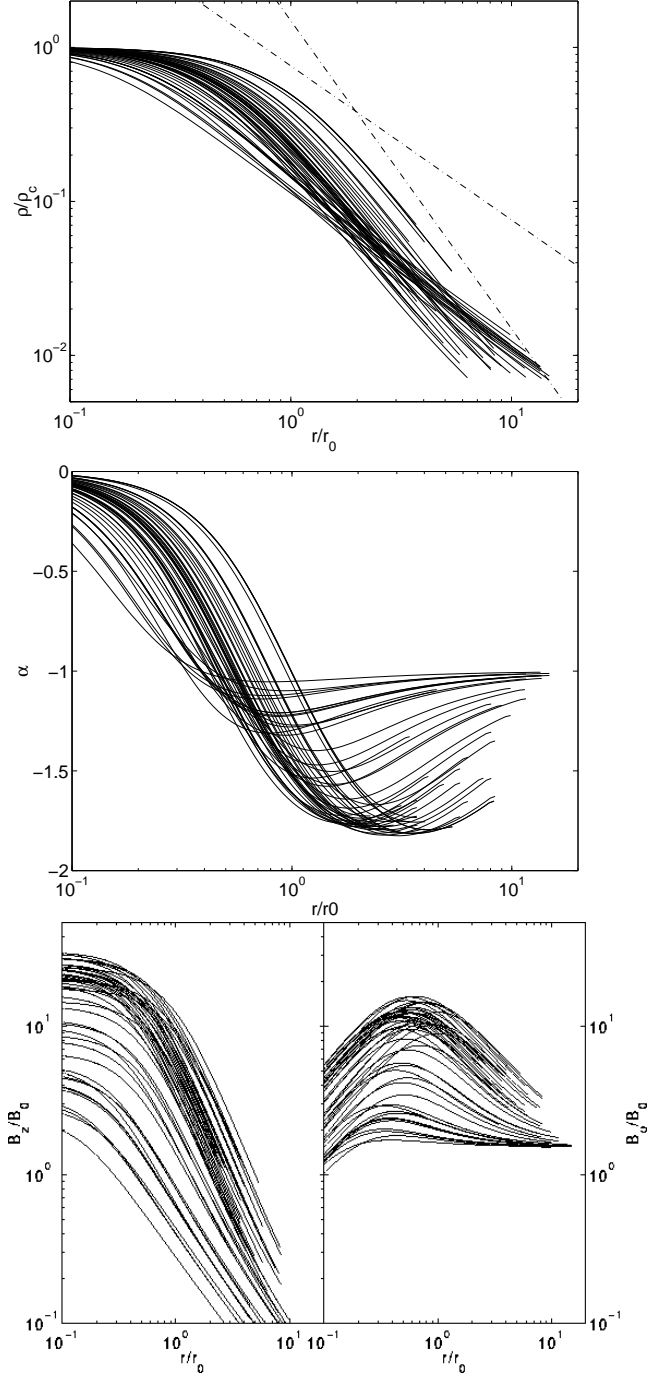


Figure 8. We show a sample of 50 logatropic models that span the range of allowed parameters given in equations 43 and 93. a) (top) We show the density profiles of the models. The dashed lines represent the r^{-4} density profile of the Ostriker solution and an r^{-2} profile, which is in agreement with the observed density profiles of filamentary clouds (Alves et al. (1998), Lada, Alves, and Lada (1998)). b) (middle) We show the how the power law index $d \ln \rho / d \ln r$ behaves with radius. c) (bottom) We show the behaviour of the poloidal and toroidal components of the magnetic field.

5 DISCUSSION

We show, in Section 2.7, that most of the filamentary molecular clouds in our sample have velocity dispersions that are too high for them to be bound by gravity and surface pressure alone. Thus, we find evidence that many filamentary clouds are probably wrapped by helical magnetic fields whose toroidal components help to confine the gas by the hoop stress of the curved field lines. It is important to realize that this conclusion is based on our virial analysis of filamentary clouds (Section 2) and is, therefore, independent of either the EOS of the gas or the mass loading of the magnetic field lines. We find that all of the filamentary clouds in our sample have masses per unit length that are much lower than the critical mass per unit length for purely hydrostatic filaments, and that filaments are quite far from their critical configurations, where $P_S/\langle P \rangle \rightarrow 0$ (See equation 43.). *Thus, star formation in filamentary clouds must involve fragmentation into periodic cores (cf. Chandrasekhar & Fermi 1953), rather than overall radial collapse.* We refer to the second paper in our series for a full analysis of this process.

We construct numerical MHD models of filamentary clouds, which we explore thoroughly in Section 4.1.3 using Monte Carlo techniques. We show that both isothermal and logtropic models are consistent with the available observational data. We find that helical fields have profound effects on the outer density profiles of filamentary clouds. While hydrostatic filaments have a density profile that falls off as r^{-4} (see Section 3.2.1), nearly all of our isothermal models with helical fields have much more shallow density profiles that fall off as $r^{-1.8}$ to r^{-2} . The toroidal component of the field is *entirely* responsible for these shallow density profiles. Logatropic models show a greater variety of behaviour, with density profiles ranging from r^{-1} to $r^{-1.8}$. We note nearly all of our isothermal models and many of our logatropic models are in excellent agreement with the r^{-2} density profiles of the filamentary clouds L977 and IC 5146, which have recently been observed by A98 and LAL98. *Helical fields must be present if the underlying EOS of filaments is isothermal, since unrealistically steep density gradients result in their absence.*

Detailed observations of real filaments are required to distinguish between the isothermal and logatropic equations of state, since both can account for the global properties of filamentary clouds. This could best be accomplished by mapping individual filaments in order to determine the radial dependence of both the surface density and the velocity dispersion. This data could be combined with our models to determine an EOS for the gas. In the absence of such data, we note that Loren (1989b) found that clumps in the filamentary clouds of Rho Ophiuchus show essentially no systematic variation of linewidth with radius; based on his study, an isothermal EOS may be most appropriate for the small filaments in Rho Ophiuchus. More concentrated filaments are not likely to be isothermal since the velocity dispersion generally increases with size. For example, observations clearly show that the velocity dispersion increases radially outward in the \int -shaped filament of Orion A (Dutrey et al. 1993).

The confirmation of helical fields in filamentary clouds will ultimately require direct observations of the field structure using sub-mm polarization and possibly molecular Zeeman

observations. Unfortunately, most polarization observations of molecular clouds have been carried out in the optical and near infra-red regions of the spectrum; Goodman et al. (1995) have demonstrated that such measurements are likely a poor indicator of magnetic field direction in cold dark clouds. More promising is the prospect of observing the thermal dust grain emission of dark clouds, which will hopefully become commonplace in the near future with instruments like the SCUBA polarimeter. In emission, we can be assured that any polarization is due to warm dust grains within the cloud being observed. Also, the lower optical depths will provide fewer difficulties due to the depolarizing effects of multiple scattering. The observational verification of our helical field models for filamentary molecular clouds will need to rely heavily on such observations.

5.1 Observational Signatures of Helical Magnetic Fields

Helical magnetic fields present an interesting and unique polarization pattern. One might naively expect to find polarization vectors aligned with some average pitch angle of the magnetic field. However, Carlqvist (1997) has modeled the polarization pattern of helical magnetic fields and demonstrated that this assumption is incorrect. The signature of a helical field, assuming that the polarization percent remains small and that the cloud is optically thin, is actually polarization vectors that are either aligned with or perpendicular to the filament axis with a possible 90° change in orientation at some radius. The reason for this counterintuitive behaviour is that any line of sight through the filament intersects a given radius not once, *but twice*. Since the order of polarizing elements is unimportant in the limit of small polarization, the combination of any symmetric pair of polarizing elements results in a cancellation of any oblique component of the net polarization. Although Carlqvist's model was done for absorption polarimetry, the same reasoning holds for emission. The overall pattern will only reflect the dominant component of the field along any line of sight; thus, our models predict that the innermost (poloidally dominated) regions of filamentary clouds should be dominated in emission by polarization vectors aligned perpendicular to the filament, while the polarization should be predominantly parallel to the filament in the (toroidally dominated) outer regions.

There is some direct evidence that filamentary clouds contain helical magnetic fields. Optical polarization and HI Zeeman data are consistent with a helical field in the large Orion A filament oriented at an approximately 20° pitch angle relative to the axis of the filament (Bally 1989). While the reliability of the optical polarization data is uncertain due to the reasons discussed above, the Zeeman observations do not suffer such ambiguity. The line of sight component of the magnetic field has been observed to *reverse* across the L1641 portion of the filament (Heiles 1987, 1989). Such a reversal is very suggestive of a helical field wrapped around the cloud. More recently, Heiles (1997) has suggested that an alternate explanation might be that the shock front of the Eridanus superbubble has swept past the Orion A cloud causing field lines to be stretched over the filament, thus simulating a helical pattern. While Heiles favours this idea, he cannot rule out the older idea that the field is intrinsically helical.

Regardless of the true nature of the \mathcal{J} -shaped filament, we observe that it is one of the few filaments shown in Figure 2 where our models do not actually require a helical field for equilibrium.

Besides the polarization and Zeeman observations, there is also some indirect evidence for helical fields. Uchida et al. (1991) have found that the velocity field of the \mathcal{J} -shaped filament is highly suggestive of gas constrained to flow in the direction of the magnetic field suggested by optical polarization. Carlqvist (1992) has observed that small filaments frequently show a tightly wound helical structure, often with intertwined helical subfilaments, arcs, and an overall sinusoidal modulation. These structures are reminiscent of structures seen in laboratory plasmas confined by toroidal magnetic fields and subject to the MHD kink instability.

5.2 The Evolution of Filamentary Molecular Clouds

An obvious interpretation of Figure 2 is that filamentary molecular clouds can be divided, theoretically, into two classes; those that are dominated by the poloidal component of the magnetic field, and those that are toroidally dominated. We find that most, but not all, of the filaments in our sample fall into the latter class. All pressure truncated, toroidally dominated filaments have masses per unit length below the critical mass per unit length m_h for unmagnetized filaments, but most poloidally dominated filaments exceed m_h due to the support of the poloidal field. *In this section, we demonstrate that the evolution of a filament is largely determined by the region of Figure 2 in which it resides.*

The evolution of an isolated filament is dominated by the effects of ambipolar diffusion and fragmentation due to gravitational instabilities. Here we consider only ambipolar diffusion. We note that a weakening of the magnetic field is represented by a decrease in $|\mathcal{M}|/|\mathcal{W}|$ in Figure 2; thus, a filament must evolve towards the dotted line in Figure 2, which represents unmagnetized equilibria. If we make the reasonable assumptions that the velocity dispersion of the filament remains constant and that the filament neither accretes additional material nor substantially changes in length, we find that m/m_{vir} is a conserved quantity during the evolution of the filament. Any evolutionary process is constrained to move a cloud along a vertical line in Figure 2. We see, therefore, that ambipolar diffusion will cause toroidally dominated filaments to decrease their internal pressures $\langle P \rangle$ by expansion until $P_S/\langle P \rangle$ reaches the unmagnetized line. On the other hand, poloidally dominated filaments with $m > m_{vir}$ cannot reach the unmagnetized line by any vertical path. Thus, a weakening of the field by ambipolar diffusion will cause $\mathcal{M}/|\mathcal{W}|$ to decrease until no equilibrium is possible. At this point, the loss of magnetic support must result in collapse.

We can estimate the timescale for ambipolar diffusion using the standard formulas (cf. McKee, Zweibel, & Goodman 1993). The mean neutral-ion collision time is given by

$$t_{ni} = (\gamma \rho_i)^{-1}, \quad (96)$$

where ρ_i is the ion density and $\gamma = 3.5 \times 10^{13} \text{ cm}^3 \text{ g}^{-1} \text{ s}^{-1}$ (Draine, Roberge, & Dalgarno 1983) is the frictional drag coefficient between ions and neutrals. Assuming equilibrium between ionization due to cosmic rays and

recombinations, the ion density is related to the neutral density ρ_n by the simple formula

$$\rho_i = C_{ion} \rho_n^{1/2}, \quad (97)$$

where $C_{ion} = 3 \times 10^{-16} \text{ cm}^{-3/2} \text{ g}^{1/2}$ (cf. Shu 1992). The neutral-ion collision time for a filament is given by

$$t_{ni} = (\gamma C_{ion} \rho^{1/2})^{-1} = \frac{\sqrt{\pi} R_S}{\gamma C_{ion} m^{1/2}}, \quad (98)$$

where we have used the excellent approximation $\rho_n \approx \rho$ and written ρ in terms of the mass per unit length m and the filament radius R_S . As we discuss in Section 4.1.2, Myers and Goodman (1988a,b) have provided considerable observational evidence that the kinetic and magnetic energy densities in molecular clouds are approximately equal. Under such equipartition, it is easy to show that $v_A \approx \sqrt{3}\sigma$. Making this approximation, we obtain a formula for the effective diffusion coefficient in filamentary molecular clouds:

$$\mathcal{D} = v_A^2 t_{ni} \approx \frac{3\sqrt{\pi}\sigma^2 R_S}{\gamma C_{ion} m^{1/2}}. \quad (99)$$

The ambipolar diffusion timescale is then given by

$$\begin{aligned} t_{A.D.} = \frac{R_S^2}{\mathcal{D}} &= \frac{\gamma C_{ion}}{3} \sqrt{\frac{2}{\pi G}} \left(\frac{m}{m_{vir}} \right)^{1/2} \frac{R_S}{\sigma} \\ &= 1.1 \times 10^7 \left(\frac{m}{m_{vir}} \right)^{1/2} \frac{R_S}{\sigma} \text{ yrs}, \end{aligned} \quad (100)$$

where R_S is in parsecs and σ is in km s^{-1} . For the small filaments in our sample, namely those of Rho Ophiuchus, we find that $t_{A.D.} \approx 2 \text{ Myr}$, while the large Northern and Southern Orion filaments have $t_{A.D.} \approx 6.6 \text{ Myr}$. The evolutionary effects of ambipolar diffusion are in competition with the tendency of a cloud to fragment due to gravitational instabilities. We compute accurate timescales for the latter in the next paper of our series.

On a final note, we consider the possibility that our helical field configurations might represent only a transient state for a filamentary cloud, since such a pattern can propagate away as a torsional Alfvén wave. The propagation speed of such a wave is similar to the velocity dispersion for clouds that are approximately in equipartition between their magnetic and kinetic energies, such as the observations require (Myers and Goodman 1988a,b). In this case the time for a wave to propagate from one end of the filament to the other is given by

$$t_A = 9.8 \left(\frac{L}{10 \text{ pc}} \right) \left(\frac{\sigma}{1 \text{ km s}^{-1}} \right)^{-1} \text{ Myr}. \quad (101)$$

On the other hand, filaments settle into radial quasi-equilibrium on a timescale which is on the order of a radial signal crossing time. Since the radius of filamentary clouds is generally a factor of at least ~ 10 smaller than the length, clouds can be expected to settle into radial equilibrium on a timescale that is shorter than t_A by the same factor. Thus, radial quasi-equilibrium is established on the order of 1 Myr for most filamentary clouds. Since this is shorter than either t_A or $t_{A.D.}$, we expect that filamentary clouds with helical fields can be approximated as quasi-equilibria, which is consistent with our analysis.

6 SUMMARY

1. All filamentary molecular clouds are truncated by external pressure that provides a total (thermal plus turbulent) pressure which is likely in the range of 10^4 to 10^5 K cm^{-3} .

2. We have derived a new form of the virial theorem appropriate for filamentary molecular clouds that are truncated by a realistic external pressure and contain ordered magnetic fields. We have collected data on filamentary clouds from the literature. We find that most of the filamentary clouds in our sample are constrained by

$$\begin{aligned} 0.11 &\lesssim m/m_{\text{vir}} \lesssim 0.43 \\ 0.012 &\lesssim P_S/\langle P \rangle \lesssim 0.75. \end{aligned} \quad (102)$$

We use these observational constraints to show that many filamentary clouds are likely wrapped by helical magnetic fields.

3. We have used our virial equation to derive virial relations for filaments that are analogous to the well-known relations for spheroidal equilibria (Chièze 1987; Elmegreen 1989; MP96). We find that the virial relations for filaments differ from the corresponding relations for spheroids only by factors of order unity.

4. We have studied the stability of filamentary molecular clouds in the sense of Bonnor and Ebert. We find that *all filamentary molecular clouds, that are initially in equilibrium, are stable against radial perturbations*. Thus, a cloud that is initially in equilibrium cannot be made to undergo radial collapse by increasing the external pressure; the only way to destabilize a filament against radial collapse is by increasing its mass per unit length beyond a critical value that depends on the magnetic field. This critical value is the maximum mass per unit length for which any equilibrium is possible; for purely hydrostatic filaments, the critical mass per unit length is given by $m_h = 2\langle\sigma^2\rangle/G$ (equation 22). The poloidal component of the magnetic field increases the critical mass per unit length by *supporting* the gas against self-gravity. The toroidal field works *with* gravity in compressing the filament; thus, the toroidal field *decreases* the critical mass per unit length.

5. There are two exact analytic solutions that can be found in the limit of vanishing magnetic field. Stodólkiewicz (1963) and Ostriker (1964) have found the equilibrium solution for unmagnetized isothermal filaments; the density in this solution tends to an $\sim r^{-4}$ behaviour outside of the core radius. A98 and LAL98 have shown that the filamentary clouds L977 and IC 5146 have density profiles that fall off as r^{-2} . If this result holds true for other filaments as well, it is unlikely that the Ostriker solution describes real molecular filaments. In addition, we have found a singular solution for unmagnetized logatropic filaments. The density profile of this filament is much more shallow; it falls off only as r^{-1} , which is probably too shallow to agree with observational results.

6. We have constructed exact numerical MHD models for filamentary clouds in Sections 4 and 4.1. We have considered both isothermal and logatropic equations of state, which likely bracket the true underlying EOS for filamentary molecular clouds. The magnetic field structure is more general than in previous studies; we have assumed only that

the poloidal and toroidal flux to mass ratios (Γ_z and Γ_ϕ) are constant, which we justify in Section 2.5.

7. Isothermal models with purely poloidal magnetic fields have density profiles that are even *steeper* than the Ostriker solution; it is unlikely that such models describe real molecular clouds. Toroidal fields result in density profiles that are more shallow than the Ostriker solution (typically r^{-2} profiles), and in better agreement with observations.

8. We have performed a Monte Carlo analysis of our models, in which we randomly sample our parameter space and then determine whether or not the resulting model agrees with the observational constraints (equations 43 and 93). We find both isothermal and logatropic filaments that are allowed by the data. We find that

$$\begin{aligned} 5 &\lesssim \Gamma_\phi \lesssim 25 \\ \Gamma_z &\lesssim 8 \end{aligned} \quad (103)$$

for isothermal filaments, and

$$\begin{aligned} 10 &\lesssim \Gamma_\phi \lesssim 40 \\ 10 &\lesssim \Gamma_z \lesssim 20 \end{aligned} \quad (104)$$

for logatropic filaments.

9. Our best-fitting isothermal models have density profiles that fall off as only $\sim r^{-1.8}$ to $\sim r^{-2}$, in contrast to the r^{-4} behaviour of the Ostriker solution. These shallow profiles are entirely due to the effects of the toroidal component of the magnetic field. *Thus, helical magnetic fields are necessary for reasonable models of isothermal filaments*. The logatropic filaments show a greater variety of density profiles that range from r^{-1} to $r^{-1.8}$. Thus, some of the logatropic filaments may agree with the observed r^{-2} profiles (A98 and LAL98), while others may be somewhat too shallow.

7 ACKNOWLEDGEMENTS

The authors wish to acknowledge Christopher McKee and Dean McLaughlin for their many insightful comments. J.D.F. acknowledges the financial support of McMaster University and an Ontario Graduate Scholarship. The research grant of R.E.P. is supported by a grant from the Natural Sciences and Engineering Research Council of Canada.

8 APPENDIX A: DERIVATION OF THE VIRIAL EQUATION FOR FILAMENTARY MOLECULAR CLOUDS

A filamentary molecular cloud may be idealized as a cylinder whose length greatly exceeds its radius. The most appropriate scalar virial equation for such an object is obtained by taking the sum of the x and y (11 and 22) diagonal components of the tensor virial equation 1; the z component can be ignored because we are concerned only with equilibrium in the *radial* direction. Considering the surface S to be the boundary of a filament of total volume V , we expand the i th diagonal component of equation 1 using the definitions 3:

$$\frac{1}{2} \frac{d^2 I_{ii}}{dt^2} = \int_V P dV - \int_S P x_i dS_i - \int_V \rho x_i \frac{\partial \Phi}{\partial x_i} dV$$

$$\begin{aligned}
& + \frac{1}{8\pi} \int_V B^2 dV - \frac{1}{4\pi} \int_V B_i^2 dV \\
& + \frac{1}{4\pi} \int_S (x_i B_i)(B_j dS_j) - \frac{1}{8\pi} \int_S B^2 x_i dS_i, \quad (105)
\end{aligned}$$

where summation over index j is implied, but *no sum is to be taken over index i* . We have also used the fact that the kinetic energy tensor T_{ik} vanishes, since the velocity is everywhere zero. Summing over components 11 and 22 and setting $\dot{I}_{11} = \dot{I}_{22} = 0$ for a filamentary cloud in equilibrium, we easily obtain

$$\begin{aligned}
0 &= 2 \int_V P dV - \int_S P \mathbf{r} \cdot d\mathbf{S} - \int_V \rho \mathbf{r} \cdot \nabla \Phi dV \\
&+ \frac{1}{4\pi} \int_V B^2 dV - \frac{1}{4\pi} \int_V (B_x^2 + B_y^2) dV \\
&+ \frac{1}{4\pi} \int_S (\mathbf{r} \cdot \mathbf{B})(\mathbf{B} \cdot d\mathbf{S}) - \frac{1}{8\pi} \int_S B^2 \mathbf{r} \cdot d\mathbf{S}, \quad (106)
\end{aligned}$$

where the position vector \mathbf{r} and surface element $d\mathbf{S}$ are defined by

$$\begin{aligned}
\mathbf{r} &= x\hat{x} + y\hat{y} \\
d\mathbf{S} &= dS_x \hat{x} + dS_y \hat{y}. \quad (107)
\end{aligned}$$

Assuming that the magnetic field is helical, it is obvious that $\mathbf{B} \cdot d\mathbf{S} = 0$; thus, the first magnetic surface term on line 3 of equation 26 is identically zero. Simplifying equation 106, we find

$$\begin{aligned}
0 &= 2 \int_V P dV - 2P_S V - \int_V \rho r \frac{\partial \Phi}{\partial r} dV \\
&+ \frac{1}{4\pi} \int_V B_z^2 dV - \frac{(B_{zs}^2 + B_{\phi s}^2)}{4\pi} V, \quad (108)
\end{aligned}$$

where we have used Gauss' theorem and the fact that $\nabla \cdot \mathbf{r} = 2$ to simplify the surface integrals. Our virial equation is obtained by dividing by the length of the filament:

$$\begin{aligned}
0 &= 2 \int P dV - 2P_S V - \int_V \rho r \frac{\partial \Phi}{\partial r} dV \\
&+ \frac{1}{4\pi} \int B_z^2 dV - \left(\frac{B_{zs}^2 + B_{\phi s}^2}{4\pi} \right) V. \quad (109)
\end{aligned}$$

It is interesting to note that this may be rewritten as

$$0 = \frac{4}{3} \mathcal{U} \left(1 - \frac{P_S}{\langle P \rangle} \right) + \mathcal{W} + \mathcal{M}, \quad (110)$$

where \mathcal{U} is the internal energy per unit length:

$$\mathcal{U} = \frac{3}{2} \int_V \rho \sigma^2 dV. \quad (111)$$

Thus, we see that our virial equation for filamentary equilibria *does* in fact differ substantially from the usual form for spheroids.

REFERENCES

- Alves J., Lada C.J., Lada E.A., Kenyon S.J., Phelps R., 1998, *Ap.J.*, 506, 292
 Bally J., 1987, *Ap.J.*, 312, L45
 Bally J., 1989, in *Proceedings of the ESO Workshop on Low Mass Star Formation and Pre-main Sequence Objects*, ed. Bo

- Reipurth; Publisher, European Southern Observatory, Garching bei Munchen
 Bateman G., 1978, "MHD Instabilities", The MIT Press, Cambridge, Massachusetts
 Bertoldi F., McKee C.F., 1992, *Ap.J.*, 395, 140
 Bonnor W.B., 1956, *MNRAS*, 116, 351
 Carlqvist P., 1998, *Ap.&S.S.*, 144, 73
 Carlqvist P., Gahm G., 1992, *IEEE Trans. on Plasma Science*, vol. 20, no. 6, 867
 Carlqvist P. & Kristen H., 1997, *A&A*, 324, 1115
 Caselli P., Myers P.C., 1995, *Ap.J.*, 446, 665
 Castets A., Duvert G., Dutrey A., Bally J., Langer W.D., Wilson R.W., 1990, *A&A*, 234, 469
 Chandrasekhar S., 1961, "Hydrodynamic and Hydromagnetic Stability", Oxford University Press, London
 Chandrasekhar S., Fermi E., 1953, *Ap.J.* 118, 116
 Chièze J.P., 1987, *A&A*, 171, 225
 Chini R., Reipurth B., Ward-Thompson D., Bally J., Nyman L.-Å., Sievers A., Billawala Y., 1997, *Ap.J.*, 474, L135
 Chromey F.R., Elmegreen, B.G., Elmegreen, D.M., 1989, *Ap.J.*, 98, 2203
 Draine B., Roberge W., Dalgarno A., 1983, *Ap.J.*, 270, 519
 Dutrey A., Duvert G., Castets A., Langer W.D., Bally J., Wilson R.W., 1993, *A&A*, 270, 468
 Dutrey A., Langer W.D., Bally J., Duvert G., Castets A., Wilson R.W., 1991, *A&A*, 247, L9
 Ebert R., 1955, *Z.Astrophys.*, 37, 217
 Elmegreen B.G., 1989, *Ap.J.*, 338, 178
 Elmegreen B.G., 1993, in *Protostars and Planets III*, ed. Levy E.H., Lunine J.I., University of Arizona Press, Tucson, Arizona
 Fuller G.A., Myers P.C., 1992, *Ap.J.*, 384, 523
 Gehman C.S., Adams F.C., Watkins R., 1996, *Ap.J.*, 472, 673
 Gomez de Castro A.I., Pudritz R.E., and Bastien P. 1997, *Ap.J.*, 476, 717
 Goodman A.A., Bastien P., Myers P.C., Ménard F., 1990, *Ap.J.*, 359, 363
 Goodman A.A., Jones T.J., Lada E.A., Myers P.C., 1995, *Ap.J.*, 448, 748
 Hanawa T., et al., 1993, *Ap.J.*, 404, L83
 Heiles C., 1987, *Ap.J.*, 315, 555
 Heiles C., 1990, *Ap.J.*, 354, 483
 Heiles C., 1997, *Ap.J.Supp.*, 111, 245
 Hildebrand R.H., 1988, *QJRAS*, 29, 327
 Inutsuka S., Miyama S.M., 1992, *Ap.J.*, 388, 392
 Lada C.J., Alves J., Lada E.A., 1998, *Ap.J.* in Press
 Loren R.B., 1989a, *Ap.J.*, 338, 902
 Loren R.B., 1989b, *Ap.J.*, 338, 925
 Maddalena R.J., Morris M., Moscovitz J., Thaddeus P., 1986, *Ap.J.*, 303, 375
 McCrea W.H., 1957, *MNRAS*, 117, 562
 McKee C.F., Zweibel E.G., Goodman A.A., Heiles C., 1993, in *Protostars and Planets III*, ed. Levy E.H., Lunine J.I., University of Arizona Press, Tucson, Arizona
 McLaughlin D.E., Pudritz R.E., 1996, *Ap.J.*, 469, 194
 Mizuno A., Onishi T., Yonekura Y., Nagahama T., Ogawa H., Fukui Y., 1995, *Ap.J.*, 445, L161
 Murphy D.C., Myers P.C., 1985, *Ap.J.*, 298, 818
 Myers P.C., Goodman A.A., 1988a, *Ap.J.*, 326, L27
 Myers P.C., Goodman A.A., 1988b, *Ap.J.*, 329, 392
 Myers P.C., Goodman A.A., Güsten R., Heiles C., 1995, *Ap.J.*, 442, 177
 Nagasawa M., 1987, *Prog. Theor. Phys.*, 77, 635
 Nakamura F., Hanawa T., Nakano T., 1993, *PASJ*, 45, 551
 Nakamura F., Hanawa T., Nakano T., 1995, *Ap.J.*, 444, 770
 Ostriker J., 1964, *Ap.J.*, 140, 1056
 Ouyed R., Pudritz R.E., 1997, *Ap.J.*, 482, 712
 Schneider S., Elmegreen B.G., 1979, *Ap.J.*, 41, 87

- Schleuning D.A., 1998, *Ap.J.*, 493, 811
Shu F.H., 1992, “The Physics of Astrophysics, Vol. II, Gas Dynamics”, University Science Books, Mill Valley, CA
Spitzer L.Jr., 1978, “Physical Processes in the Interstellar Medium”, John Wiley & Sons, New York
Stodólkiewicz J.S., 1963, *Acta Astron.*, 13, 30
Strittmatter P.A., 1966, *MNRAS*, 132, 359
Uchida Y., Fukui Y., Mizuno A., Iwata T., Takaba H., 1991, *Nature*, 349, 140
Ungerechts H., Thaddeus P., 1987, *Ap.J.Supp.*, 63, 645
Viala Y.P., Horedt Gp., 1974, *A&A*, 33, 195